



The Type II-P Supernova 2017eaw: From Explosion to the Nebular Phase

Tamás Szalai^{1,2}, József Vinkó^{1,2,3}, Réka Könyves-Tóth², Andrea P. Nagy^{1,2}, K. Azalee Bostroem⁴,
Krisztián Sárnecky², Peter J. Brown⁵, Ondrej Pejcha⁶, Attila Bódi^{2,18}, Borbála Cseh², Géza Csörnyei², Zoltán Dencs²,
Ottó Hanyecz², Bernadett Ignácz², Csilla Kalup^{2,18}, Levente Kriskovics², András Ordasi², András Pál², Bálint Seli²,
Ádám Sódor^{2,18}, Róbert Szakáts², Krisztián Vida², Gabriella Zsidi²

Konkoly team,

and

Iair Arcavi⁷, Chris Ashall^{8,9}, Jamison Burke^{10,11}, Lluís Galbany¹², Daichi Hiramatsu^{10,11}, Griffin Hosseinzadeh^{10,11,13},
Eric Y. Hsiao⁹, D. Andrew Howell^{10,11}, Curtis McCully^{10,11}, Shane Moran¹⁴, Jeonghee Rho¹⁵, David J. Sand¹⁶,
Melissa Shahbandeh⁹, Stefano Valenti⁴, Xiaofeng Wang¹⁷, and J. Craig Wheeler³

Global Supernova Project

¹ Department of Optics and Quantum Electronics, University of Szeged, Dóm tér 9, Szeged, 6720 Hungary; szaszi@titan.physx.u-szeged.hu

² Konkoly Observatory, Research Centre for Astronomy and Earth Sciences, Hungarian Academy of Sciences, H-1121 Budapest, Hungary

³ Department of Astronomy, University of Texas at Austin, Austin, TX 78712, USA

⁴ Department of Physics, University of California, Davis, CA 95616, USA

⁵ George P. and Cynthia Woods Mitchell Institute for Fundamental Physics and Astronomy, Texas A&M University, Department of Physics and Astronomy, 4242 TAMU, College Station, TX 77843, USA

⁶ Institute of Theoretical Physics, Faculty of Mathematics and Physics, Charles University in Prague, Czech Republic

⁷ The School of Physics and Astronomy, Tel Aviv University, Tel Aviv 69978, Israel

⁸ Astrophysics Research Institute, Liverpool John Moores University, IC2, Liverpool Science Park, 146 Brownlow Hill, Liverpool L3 5RF, UK

⁹ Department of Physics, Florida State University, 77 Chieftan Way, Tallahassee, FL 32306, USA

¹⁰ Las Cumbres Observatory, 6740 Cortona Drive, Suite 102, Goleta, CA 93117-5575, USA

¹¹ Department of Physics, University of California, Santa Barbara, CA 93106-9530, USA

¹² PITT PACC, Department of Physics and Astronomy, University of Pittsburgh, Pittsburgh, PA 15260, USA

¹³ Center for Astrophysics, Harvard & Smithsonian, 60 Garden Street, Cambridge, MA 02138, USA

¹⁴ Tuorla Observatory, Department of Physics and Astronomy, University of Turku, Väisäläntie 20, FI-21500 Piikkiö, Finland

¹⁵ SETI Institute, 189 North Bernardo Avenue, Suite 200, Mountain View, CA 94043, USA

¹⁶ Department of Astronomy/Steward Observatory, 933 North Chery Avenue, Room N204, Tucson, AZ 85721-0065, USA

¹⁷ Physics Department and Tsinghua Center for Astrophysics (THCA), Tsinghua University, Beijing, 100084, People's Republic of China

¹⁸ MTA CSFK Lendület Near-Field Cosmology Research Group

Received 2019 January 28; revised 2019 March 4; accepted 2019 March 21; published 2019 April 29

Abstract

The nearby SN 2017eaw is a Type II-P (“plateau”) supernova (SN) showing early-time, moderate CSM interaction. We present a comprehensive study of this SN, including the analysis of high-quality optical photometry and spectroscopy covering the very early epochs up to the nebular phase, as well as near-ultraviolet and near-infrared spectra and early-time X-ray and radio data. The combined data of SNe 2017eaw and 2004et allow us to get an improved distance to the host galaxy, NGC 6946, of $D \sim 6.85 \pm 0.63$ Mpc; this fits into recent independent results on the distance of the host and disfavors the previously derived (30% shorter) distances based on SN 2004et. From modeling the nebular spectra and the quasi-bolometric light curve, we estimate the progenitor mass and some basic physical parameters for the explosion and ejecta. Our results agree well with previous reports on a red supergiant progenitor star with a mass of $\sim 15\text{--}16 M_{\odot}$. Our estimation of the pre-explosion mass-loss rate ($\dot{M} \sim 3 \times 10^{-7}\text{--}1 \times 10^{-6} M_{\odot} \text{ yr}^{-1}$) agrees well with previous results based on the opacity of the dust shell enshrouding the progenitor, but it is orders of magnitude lower than previous estimates based on general light-curve modeling of Type II-P SNe. Combining late-time optical and mid-infrared data, a clear excess at $4.5 \mu\text{m}$ can be seen, supporting the previous statements on the (moderate) dust formation in the vicinity of SN 2017eaw.

Key words: supernovae: general – supernovae: individual (SN 2017eaw)

1. Introduction

Recently, the growing number of well-observed (i.e., having high signal-to-noise ratio, high-cadence data spanning a wide wavelength range) Type II supernovae (SNe II) revealed important new details about their progenitors, explosion mechanisms, and diversity (see, e.g., Valenti et al. 2016, and references therein). For example, photometry and spectroscopy taken at the earliest phases, during and after shock breakout, turned out to be especially useful for constraining the progenitor radii and/or probing the nearby circumstellar matter (Garnavich et al. 2016; Khazov et al. 2016).

P. Wiggins discovered SN 2017eaw on UT 2017 May 14.238 at a brightness of 12.8 mag (Wiggins 2017). Within a few hours, the presence of the new transient was confirmed by Dong & Stanek (2017) based on images taken by the Las Cumbres Observatory (LCO) 1 m telescope at McDonald Observatory, Texas. The object was first classified as a young Type II SN (Cheng et al. 2017; Tomasella et al. 2017), while, soon after, Xiang et al. (2017) found that the early spectra of SN 2017eaw match well with those of young Type II-P explosions; later, the classification was confirmed by photometry.

The object appeared in NGC 6946, at $61^{\circ}0'$ west and $143^{\circ}0'$ north of the center of the galaxy. The host is a nearby, face-on spiral galaxy, which has produced around a dozen known SNe and other luminous transients, including the Type II-L SN 1980K; Type II-P SNe 1948B, 2002hh, and 2004et; and SN impostor 2008S. The first precise astrometric position of SN 2017eaw, based on ground-based imaging, was given by Sárneczky et al. (2017): $\alpha = 20^{\text{h}}34^{\text{m}}44^{\text{s}}.238$, $\delta = +60^{\text{d}}11^{\text{m}}36^{\text{s}}.00$ (with rms uncertainties of $\Delta\alpha = 0''.08$ and $\Delta\delta = 0''.09$). Later, Kilpatrick & Foley (2018) determined a very similar, even more precise position of the object on post-explosion *Hubble Space Telescope* (*HST*) images: $\alpha = 20^{\text{h}}34^{\text{m}}44^{\text{s}}.272$, $\delta = +60^{\text{d}}11^{\text{m}}36^{\text{s}}.008$ (with an uncertainty of $\sim 0''.002$ – $0''.003$ in both α and δ).

Since SN 2017eaw is one of the closest core-collapse (CC) SNe to date and appeared in a host galaxy that is being monitored almost continuously, the search for the potential progenitor in archival imaging data was started right after the announcement of discovery. The first hints of a possible progenitor were reported by Khan (2017; based on mid-infrared *Spitzer Space Telescope* images), Drake et al. (2017; based on optical Catalina Sky Survey images), and van Dyk et al. (2017; using *HST* ACS/WFC F814W images); all of these findings suggested the presence of a red supergiant (RSG) star at the position of the SN. The detailed analysis by Kilpatrick & Foley (2018), based on archival *HST* and *Spitzer* images, confirmed the RSG progenitor ($\log(L/L_{\odot}) = 4.9$, $T_{\text{eff}} = 3350$ K, $M_{\text{ini}} = 13 M_{\odot}$) obscured by a dust shell; these results agree well with those of Rui et al. (2019) based on a similar analysis. In the frameworks of comprehensive studies, two other groups also published their findings on the progenitor candidate of SN 2017eaw. Williams et al. (2018) carried out an age-dating study of the surrounding stellar populations of nearby (historic) CC SNe on new *HST* images; based on that, they derived a somewhat smaller mass for the assumed progenitor of SN 2017eaw ($\sim 9 M_{\odot}$). Johnson et al. (2018) presented the results of long-term multichannel optical monitoring of the progenitors of Type II SNe; they found a general brightness variability smaller than 5%–10%, which is in agreement with the known properties of RSG stars.

Since its early phase, SN 2017eaw has been the target of several multiwavelength observing campaigns; however, only a few data sets have been published to date. Tsvetkov et al. (2018) presented the results of their *BVRI* photometric campaign covering the first ~ 200 days. Rho et al. (2018) obtained and analyzed near-infrared (near-IR) spectra spanning the time interval 22–205 days after discovery, while Kilpatrick & Foley (2018) published only a single optical spectrum taken during the photospheric phase. Radio and X-ray (non) detections have also been reported (see Section 4.2).

In this paper, we present a comprehensive study of the early- and late-time properties of SN 2017eaw. First, we present our ground-based spectroscopic and photometric observations in Section 2. After that, we give the details of the comparison of the light curves (LCs) and spectra with those of other SNe II-P, the extraction of physical parameters from bolometric LC modeling, and the estimation of the distance of the host galaxy based on the combined data of SNe 2017eaw and 2004et. We also present our findings from the analysis of early-time radio and X-ray (non)detections and the late-time mid-infrared data of SN 2017eaw and interpret these as potential signs of circumstellar interaction and dust formation in the vicinity of

the explosion site, respectively. In Section 4, we discuss our results, and finally, in Section 5, we present our conclusions.

2. Observations

This section contains the description of the observational data on SN 2017eaw collected with various ground- and space-based instruments. All data will be publicly released via WiseREP.¹⁹

2.1. Photometry

Ground-based photometric observations for SN 2017eaw were obtained from the Piszkestető Mountain Station of Konkoly Observatory, Hungary. We used the 0.6/0.9 m Schmidt telescope with the attached liquid-cooled FLI Proline PL16801 4096 \times 4096 CCD (FoV 70×70 arcmin²) equipped with Bessell *BVRI* filters. The CCD frames were bias-, dark-, and flat-field-corrected by applying standard IRAF²⁰ routines. To obtain the Konkoly *BVRI* magnitudes, we carried out point-spread function (PSF) photometry on the SN and five local comparison (tertiary standard) stars using the `allstar` task in IRAF. We applied an aperture radius of $6''$ and a background annulus from $7''$ to $10''$ for SN 2017eaw, as well as for the local comparison stars. The magnitudes of the local comparison stars were determined from their PS1 photometry after transforming the PS1 *gri* magnitudes to the Johnson–Cousins *BVRI* system.

Long-term photometric data were collected as part of the Global Supernova Project by the LCO. Using `lco_gtsnpipe` (Valenti et al. 2016), a PyRAF-based photometric reduction pipeline, we measured the PSF photometry of the SN. Because the SN is well separated from its host galaxy, image subtraction is not required. Local-sequence stars were calibrated to $g'r'i'$ *AB* magnitudes from the APASS catalog (Henden et al. 2015) and to standard fields (e.g., L113) observed on the same night at the same observatory site using *UBV* magnitudes from Landolt (1992).

The ground-based optical observations were supplemented by the available *Neil Gehrels Swift Observatory* (hereafter *Swift*; Gehrels et al. 2004; Burrows et al. 2005) data taken with the Ultraviolet-Optical Telescope (UVOT; Roming et al. 2005) and reduced using standard HEASoft tasks. Individual frames were summed with the `uvotimsum` task. Magnitudes were determined via aperture photometry using the task `uvotsource` and adopting the most recent zero-points (Breeveld et al. 2011).

The results of our LCO *UBVg'r'i'* (in Vega magnitudes for *UBV* and *AB* magnitudes for $g'r'i'$), Konkoly *BVRI*, and *Swift* photometry (both in Vega magnitudes) are shown in Figure 1; the data are also presented in Tables 4–6 in the Appendix, respectively. Intrinsic photometric errors are typically below 0.05 mag, while the overlapping photometric data sets—LCO/Konkoly/*Swift* *BV* magnitudes, as well as our *BVRI* data and those of Tsvetkov et al. (2018)—are generally consistent within ~ 0.1 mag.

2.2. Spectroscopy

A number of low-resolution optical spectra ($R \sim 400$ – 700 in the 370–1050 nm range) were collected at LCO sites using the

¹⁹ <https://wiserep.weizmann.ac.il>

²⁰ IRAF is distributed by the National Optical Astronomy Observatories, which are operated by the Association of Universities for Research in Astronomy, Inc., under cooperative agreement with the National Science Foundation.

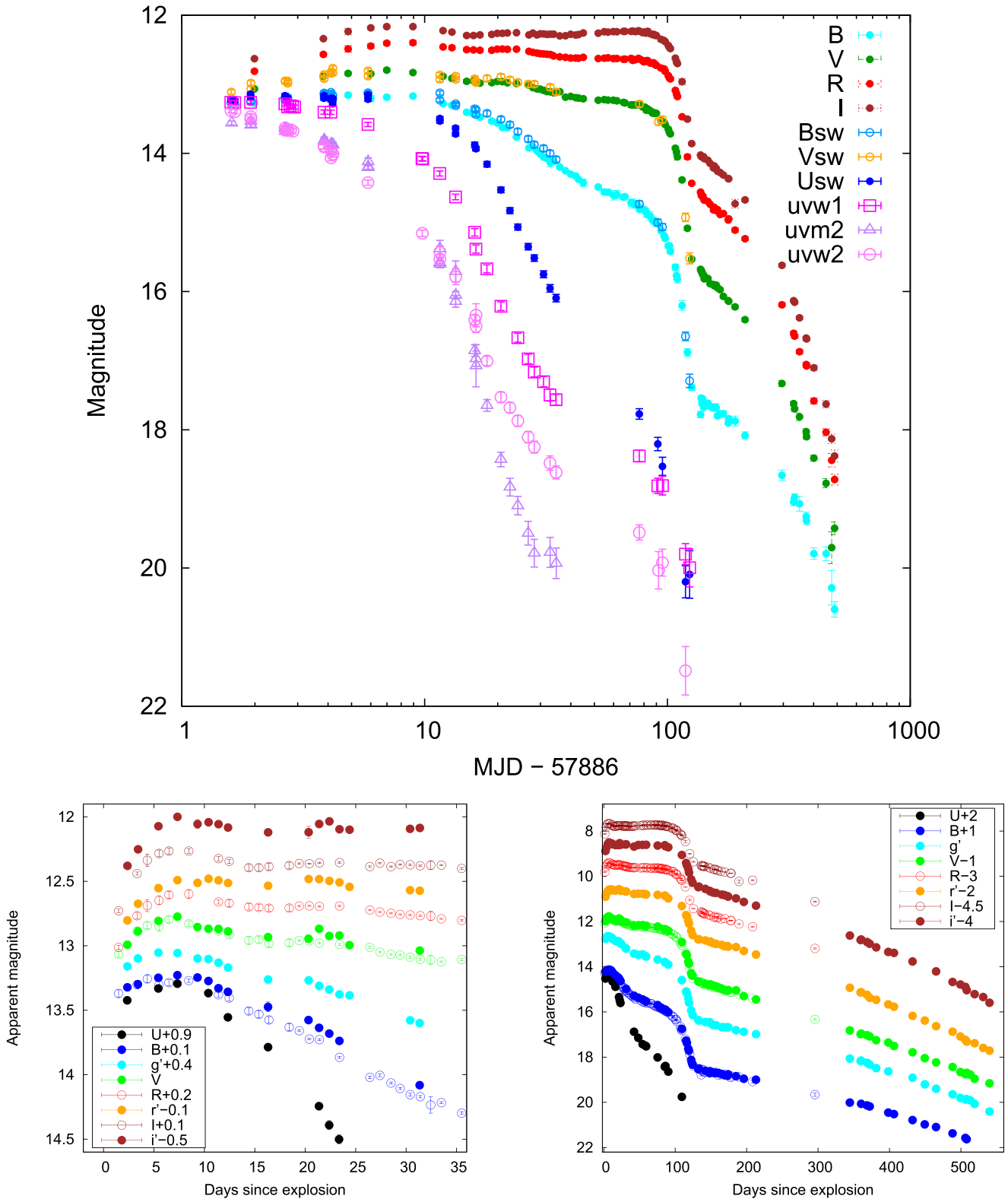


Figure 1. Top panel: multicolor LCs of SN 2017eaw from Konkoly and *Swift*/UVOT. The *Swift* UV data have been shifted by +1 mag for better visibility. Bottom panels: Konkoly *BVRI* (open circles) and LCO *UBVg'r'i'* (filled circles) photometric data during the first month (left) and up to +545 days (right).

FLOYDS instruments. Additionally, a sequence of optical spectra on SN 2017eaw was taken with the Low Resolution Spectrograph 2 (LRS2) mounted on the 10 m Hobby–Eberly Telescope (HET). The LRS2 consists of two dual-arm spectrographs covering the 370–470 and 460–700 nm region

(LRS2-B UV and orange arms) and the 650–842 and 818–1050 nm region (LRS2-R red and IR arms), respectively, with an average spectral resolution of about 1500 (Chonis et al. 2016). Both arms are fiber-fed by their own integral field unit having 280 fibers packed densely to fully cover a 12×6 arcsec²

field of view. For further details on the instrument and data reduction, see, e.g., Li et al. (2019).

Swift took two near-ultraviolet (near-UV) spectra with UVOT/UGRISM covering the 200–500 nm regime. These data were downloaded from the Swift Data Archive²¹ and extracted using the HEASoft task *uvotimgrism*.

Furthermore, five near-IR spectra were taken with the 3.0 m NASA Infrared Telescope Facility (IRTF) and the SpeX spectrograph (Rayner et al. 2003). The data were taken in “SX-D” mode, with wavelength coverage from ~ 0.8 to $2.4 \mu\text{m}$, cross-dispersed into six orders. The observations were taken using the classic ABBA technique for improved sky subtraction, and an A0V star was observed for telluric correction. For further details of the observational setup and execution, see Hsiao et al. (2019). The data were reduced using the publicly available SPEXTOOL software package (Cushing et al. 2004), and the telluric corrections were performed with the XTELLCOR software suite (Vacca et al. 2003).

Optical spectra were obtained during the nebular phase on days 220, 435, and 491. The first spectrum was taken on 2017 December 19.23 UT with the Low Resolution Imaging Spectrometer (LRIS; Oke et al. 1995; McCarthy et al. 1998; Rockosi et al. 2010) at the 10 m W. M. Keck Observatory (2017B, project code U109, PI: Valenti). The spectrum was taken using a $1''$ aperture with the 560 dichroic to split the beam between the 600/4000 grism on the blue side and the 400/8500 grating on the red side. Taken together, the merged spectrum spans ~ 3200 – 10200 \AA . Data were reduced in a standard way using the LPIPE pipeline.²² The remaining spectra were observed on 2018 July 22.52 UT and 2018 September 16.31 UT with the Gemini Multi-Object Spectrograph (GMOS; Hook et al. 2004; Gimeno et al. 2016) mounted on the 8 m Frederick C. Gillett Gemini-North telescope (program ID: GN-2018B-Q-204; PI: Bostroem). Observations were taken using a $1''$ aperture utilizing a red setup and a blue setup to obtain wavelength coverage from 3450 to 9900 \AA . The red setup observations were taken with the R400 grating and the OG515 blocking filter with a resolution of $R \sim 1918$. The blue setup observations were taken with the B600 grating with a resolution of $R \sim 1688$. The spectra were reduced using a combination of the Gemini *iraf* package and custom Python scripts.²³ Extracted spectra were scaled to photometry interpolated or extrapolated to the date of observation.

The journal of all spectroscopic observations is given in Table 7 in the Appendix. The sequence of optical spectra is plotted in Figure 2, while the detailed analysis of all optical, near-UV, and near-IR spectra is presented in Section 3.

3. Analysis and Results

First, we estimate some basic parameters of SN 2017eaw: the moment of explosion (t_0), the interstellar extinction toward the SN, and the distance to the host galaxy.

We adopt $t_0 = 2,457,886.5 \pm 1.0 \text{ JD}$ (May $13.0 \pm 1.0 \text{ UT}$) as the moment of explosion of SN 2017eaw. This value is strengthened by our distance estimation analysis (see Section 3.3) and suits well both the date of discovery (2017 May 14.2) and the epoch of last nondetection (2017 May 12.2).

Finding the true value of the total extinction in the line of sight of SN 2017eaw does not seem to be trivial. Using the reddening map of Schlafly & Finkbeiner (2011), we get $E(B - V)_{\text{gal}} = 0.30 \text{ mag}$ for the Galactic extinction. For the total extinction, several estimates based on empirical relations between the total reddening and equivalent widths (EWs) of Na I D lines exist in the literature: for example, Tomasella et al. (2017) derived $E(B - V)_{\text{tot}} = 0.22 \text{ mag}$ for the total (Galactic + host) extinction using the formulae by Turatto et al. (2003), which is lower than the Galactic component given above, while Kilpatrick & Foley (2018) determined $E(B - V)_{\text{tot}} = 0.34 \text{ mag}$ following the method of Poznanski et al. (2012).

The $\sim 0.1 \text{ mag}$ difference between these two estimates illustrates the issue that these empirical relations may suffer from relatively high systematic errors (see, e.g., Blondin et al. 2009; Poznanski et al. 2011; Faran et al. 2014). This belief is confirmed by our own analysis. Based on our HET spectra, we also determined the EWs of the Na I D1 and D2 features, as well as those of the combined line profile (D1+D2), as 0.8, 1.1, and 1.7 \AA , respectively. Because of the very low redshift of SN 2017eaw, the Na I D doublet at 5890–5895 \AA originating from the Milky Way may be blended with the same features formed in the interstellar medium of the host galaxy (and maybe in the CSM around the SN site). In any case, such high EW values would imply $E(B - V) > 1 \text{ mag}$ according to the empirical relations given by Poznanski et al. (2012). Since the $\text{EW}(\text{Na I}) - E(B - V)$ relation is suspected to saturate at $E(B - V) \gtrsim 0.2 \text{ mag}$, these measurements probably overestimate the total reddening toward SN 2017eaw.

Diffuse interstellar band (DIB) features offer an independent and sometimes more reliable way to estimate the interstellar reddening. In the same HET spectrum as above, we measured the EW of the unresolved blend of the Galactic and host DIB 5780 \AA feature and got $\sim 0.31 \text{ \AA}$. Repeating the same measurement but using a public spectrum of SN 2004et, a Type II-P SN that occurred in the same host galaxy, resulted in $\text{EW}(\text{DIB}) \sim 0.19 \text{ \AA}$ (see Figure 3). These values correspond to $E(B - V) \sim 0.52$ and $\sim 0.32 \text{ mag}$, respectively, following Phillips et al. (2013), who applied the method by Friedman et al. (2011).

For SN 2004et, Zwitter et al. (2004) determined $E(B - V)_{\text{tot}} = 0.41 \text{ mag}$ based on the method of Munari & Zwitter (1997), which was also adopted by Maguire et al. (2010). Since the optical spectra of SNe 2017eaw and 2004et appear to be very similar (see Section 3.2), including Na D profiles, and this $E(B - V)$ value is close to the mean of the results from the various estimates detailed above, in the rest of this paper, we adopt and use $E(B - V)_{\text{tot}} = 0.41 \text{ mag}$ as the total reddening toward SN 2017eaw, but we note that the uncertainty of this value is at least $\pm 0.1 \text{ mag}$, as explained above.

Similarly, we use $D = 6.85 \pm 0.63 \text{ Mpc}$ for the distance of the host galaxy that comes from our own detailed analysis using various methods and the combination of other recently published distances to NGC 6946 (see Section 3.3).

In the following, we present a detailed photometric and spectroscopic study of SN 2017eaw, comparing the results with those of several other Type II-P SNe (see Table 1). All of the fluxes were dereddened using the Galactic reddening law parameterized by Fitzpatrick & Massa (2007) assuming $R_V = 3.1$.

²¹ <https://swift.gsfc.nasa.gov/archive/>

²² <http://www.astro.caltech.edu/dperley/programs/lpipe.html>

²³ <https://github.com/cmccully/lcogtgemini>

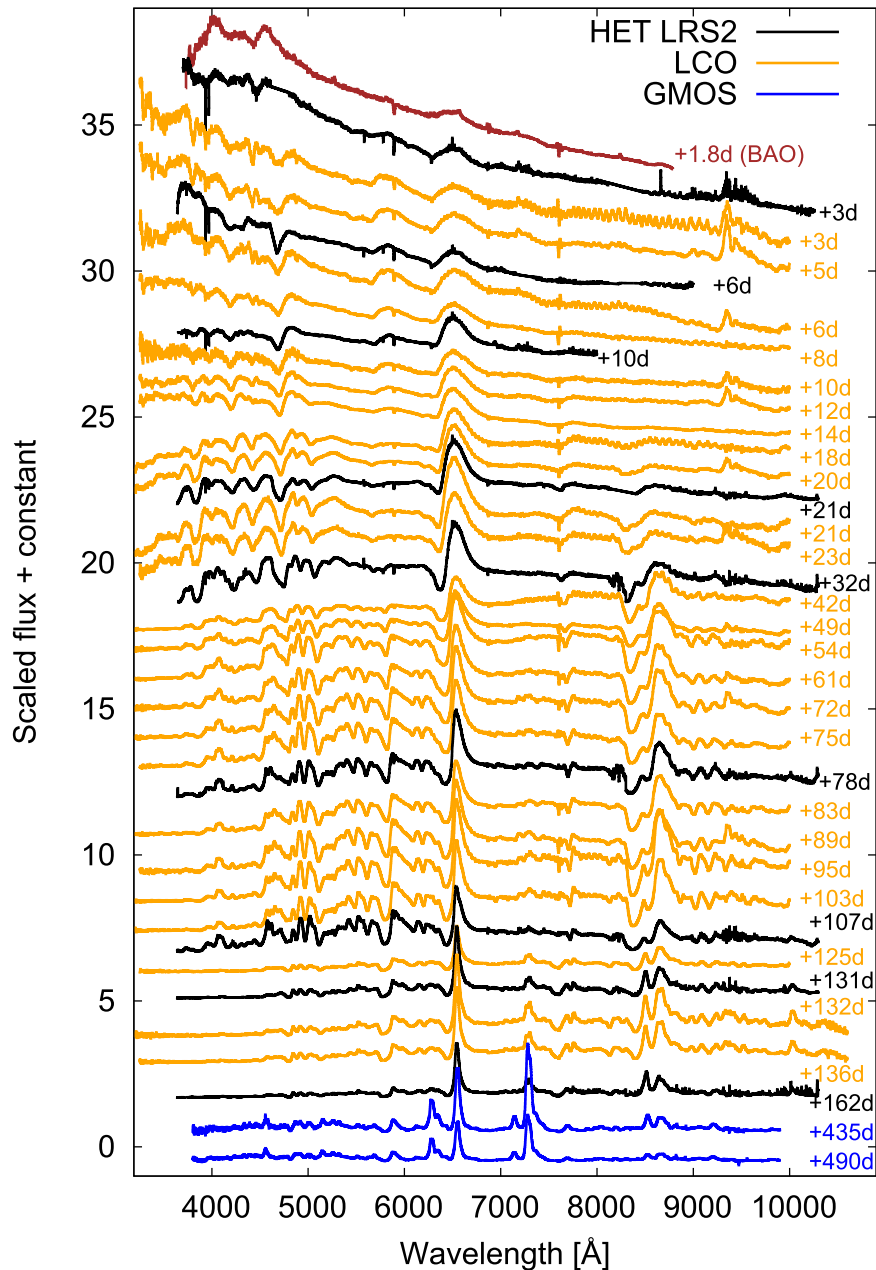


Figure 2. Optical spectra of SN 2017eaw obtained with HET LRS2 (black) and Gemini-North GMOS-N (blue) and from LCO sites (orange). An additional public spectrum (downloaded from WiSERep, <https://wiserep.weizmann.ac.il>) obtained on May 14 from the Beijing Astronomical Observatory (BAO) is also shown (brown).

3.1. Photometric Comparison

We have selected several recent, well-observed Type II-P SNe for both photometric and spectroscopic comparison, including “normal” (but slightly superluminous) Type II-P SN 2004et (that appeared in the same host as SN 2017eaw), “normal” (but slightly subluminal) SN 2012aw, early-caught and strongly interacting SN 2013fs, early-caught and slightly subluminal SN 2016X, and early-time interacting, subluminal SN 2016bkv. Table 1 lists the basic data of the selected objects, as well as their references.

Figures 4 and 5 show the early-time and long-term absolute *BVRI* LCs of SN 2017eaw, together with that of the other selected SNe, respectively (absolute magnitudes were calculated using the distances and reddening values presented in

Table 1). As can be seen in Figure 4, SN 2017eaw shows a small, early bump peaking at $\sim 6\text{--}7$ days after explosion in all optical channels. This behavior resembles quite well that of SN 2013fs and is supposed to be the sign of early-time circumstellar interaction (Morozova et al. 2017, 2018; Yaron et al. 2017; Bullivant et al. 2018); this topic is further analyzed in Section 4.2.

After the early, small bump, SN 2017eaw shows a long plateau up to ~ 100 days, just as “normal” SNe II-P (e.g., 2004et), which probably indicates that the masses of the H envelopes are similar in these cases (unlike SN 2013fs, whose plateau drops ~ 25 days earlier).

In Figure 6, we present the reddening-corrected color curves of a sample of SNe II-P. Basically, SN 2017eaw seems to

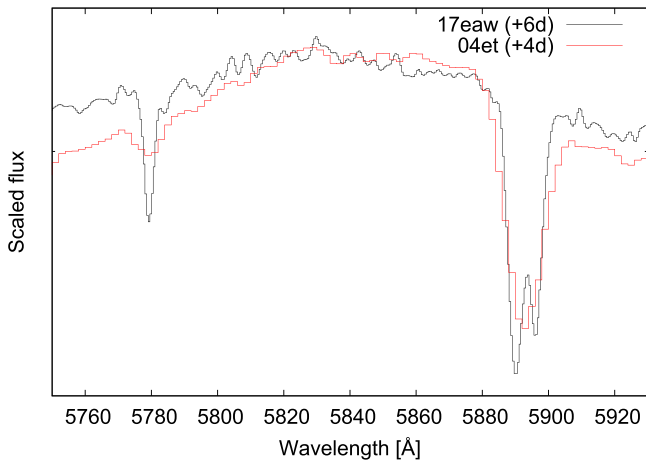


Figure 3. Region of DIB 5780 Å and Na I D1 and D2 lines on both the +6 day HET spectrum of SN 2017eaw and the +4 day spectrum of SN 2004et (see the text regarding the estimation of total extinction in Section 3).

follow the color evolution of other SNe II-P. The $(B - V)_0$ color is quite blue in the early phases but evolves relatively rapidly toward redder colors as the ejecta expands and cools; at ~ 125 days, there is a transition peak, after which the $(B - V)_0$ color becomes gradually bluer. The $(V - R)_0$ and $(V - I)_0$ evolve more slowly, and these curves become relatively flat after ~ 125 days (in part because in this phase, the SN II photometric evolution, which depends on the ^{56}Co decay, is approximately the same in all bands; see, e.g., Galbany et al. 2016). Nevertheless, we note that, on one hand, the color data are quite uncertain for most of the selected SNe after ~ 100 days (sometimes there are no data at all), and, on the other hand, the reddening of several SNe—including 2017eaw and 2004et—is somewhat uncertain (as we described above).

3.2. Spectroscopic Comparison

Based on our observational data set on SN 2017eaw and published data on other Type II-P SNe listed in Table 1, we carried out a detailed comparative spectroscopic analysis. First, all observed spectra were corrected for the recession velocity of their host galaxies and the total reddening/extinction listed in Table 1.

3.2.1. Optical Spectra

In Figure 7, we present the comparison of the optical spectra of SN 2017eaw with those of other SNe used above for the photometric comparison, selecting three ranges of epochs: 2–6, 28–35, and 78–84 days (upper left, upper right, and bottom panels, respectively; data sources are listed in Table 1). In general, the spectral evolution of SN 2017eaw follows the same trend that can usually be seen in Type II-P SNe; however, minor differences can also be found among the spectra.

The differences are most apparent during the early days. Both SNe 2013fs (Yaron et al. 2017; Bullivant et al. 2018) and 2016bkv (Hosseinzadeh et al. 2018; Nakaoka et al. 2018) have been found to exhibit a short-lived but intense circumstellar interaction: they showed numerous narrow emission lines during the first few days after explosion. At the same time, neither SN 2016X (Huang et al. 2018) nor SN 2017eaw showed any similar phenomena, even though an early-time moderate CSM interaction may have taken place in 2017eaw

(see also Section 4.2), similar to the “normal” Type II-P SNe 2004et and 2012aw (we note that, based on a very recent paper of Rui et al. 2019, a weak narrow $\text{H}\alpha$ line was observed in the 1.4 day spectrum of SN 2017eaw). At ~ 3 months, all spectra look very similar to each other, except those of the low-luminosity SN 2016bkv, which shows much weaker $\text{H}\alpha$ and Ca II features and some further incredibly narrow features compared to other objects. Note that while SNe 2017eaw, 2004et, and 2012aw are all in the plateau phase at this time, SN 2013fs is already in the declining phase, while in the case of SN 2016bkv, LC sampling is too poor to observe the transition (see Figure 5).

The spectral similarity between SNe 2017eaw, 2004et, and 2012aw is even more pronounced when their spectrum models, computed with SYNOW, are compared. Because SYNOW models for it are available (Bose et al. 2013), SN 2012aw is selected as a reference. We adopted this model sequence for identifying the main features in the spectra of SN 2017eaw at three selected epochs (see Figure 8). As can be seen, all of the key spectral features appear with very similar line strengths in both spectra, except maybe $\text{H}\beta$ at the earliest epoch and Si II 6355 Å, which seems to be somewhat stronger and at a higher velocity in the +78 day spectrum of SN 2017eaw than in SN 2012aw.

3.2.2. Velocity Determination

Using our optical spectra, we also determined the $\text{H}\beta$ and Fe II 5169 Å line velocities for SN 2017eaw ($v_{\text{H}\beta}$ and $v_{\text{Fe II}}$, respectively) up to +85 days. For calculating $v_{\text{H}\beta}$ and $v_{\text{Fe II}}$ values, taking advantage of the adequate signal-to-noise ratio of both HET and LCO spectra, we simply fitted single Gaussian profiles to the regions of the absorption minima of the two lines.

Before +20 days, $\text{H}\beta$ is the most appropriate feature for velocity determination; later, $v_{\text{H}\beta}$ and its uncertainties become higher because of the increasing optical depth of $\text{H}\beta$, as well as the blending with Ti II, Fe II, and Ba II features.

After +20 days, $v_{\text{Fe II}}$ is thought to be a good indicator of the photospheric velocity (v_{phot}), since the minimum of the Fe II 5169 Å absorption profile tends to form near the photosphere (see Branch et al. 2003); however, the detailed investigation of Takáts & Vinkó (2012) showed that the true v_{phot} may significantly differ from single line velocities. Nevertheless, in the case of SN 2012aw, the spectral modeling obtained by Bose et al. (2013) shows that v_{phot} can be well estimated with $v_{\text{H}\beta}$ and $v_{\text{Fe II}}$ before and after +20 days, respectively. Thus, based on the high spectral similarity of the two objects, we assume that this estimation is also feasible in the case of SN 2017eaw.

Figure 9 shows the results compared to the line velocities of SNe 2004et (Takáts & Vinkó 2012) and 2012aw (Bose et al. 2013). It is interesting that, despite the spectral similarities mentioned above, SN 2017eaw seems to have a $\lesssim 1000 \text{ km s}^{-1}$ systematically higher $v_{\text{Fe II}}$ than either SN 2004et or SN 2012aw. On the other hand, the $v_{\text{H}\beta}$ velocities for SN 2017eaw are lower than those of SN 2004et after +25 days. As shown in previous studies (see, e.g., Takáts & Vinkó 2012; Faran et al. 2014, and references therein), the Fe II 5169 Å and H line velocities evolve as $v(t)/v(50) = (t/50)^{-\beta}$ in SNe II-P. Repeating this fitting to SN 2017eaw, we get $\beta = 0.567 \pm 0.021$ and 0.499 ± 0.020 for $v_{\text{Fe II}}$ and $v_{\text{H}\beta}$, respectively, which are in good agreement with previous results. Moreover, we also plot $v_{\text{Fe II}}$ against $v_{\text{H}\beta}$

Table 1
Basic Data of Type II-P SNe Used for Comparison

Name	Host Galaxy	Date of Explosion (JD−2,400,000)	z	D (Mpc)	$E(B - V)_{\text{tot}}$ (mag)	Source
SN 2017eaw	NGC 6946	57,886.5 ± 1.0	0.00013	6.85 ± 0.63	0.41	(1), (2)
SN 2004et	NGC 6946	53,270.5 ± 1.0	0.00013	6.85 ± 0.63	0.41	(1), (2)
SN 2012aw	NGC 3351	56,002.6	0.00260	9.9 ± 0.1	0.07	(3)
SN 2013fs	NGC 7610	56,571.1	0.01190	51.0 ± 3.0	0.05	(4)
SN 2016X	UGC 08041	57,405.9	0.00441	15.2 ± 2.0	0.04	(5)
SN 2016bkv	NGC 3184	57,467.5	0.00198	14.4 ± 0.3	0.01	(6), (7)

Note. Parameters marked with boldface have been determined in this work. Redshifts are adopted from NED (<https://ned.ipac.caltech.edu>).

References. (1) This work, (2) Maguire et al. (2010), (3) Bose et al. (2013), (4) Yaron et al. (2017), (5) Huang et al. (2018), (6) Hosseinzadeh et al. (2018), (7) Nakaoka et al. (2018).

(Figure 9, right panel) and get a linear relation with a slope of 0.853 ± 0.016 , which agrees well with that of other SNe II-P (see, e.g., Poznanski et al. 2010; Takáts & Vinkó 2012; Faran et al. 2014; Gall et al. 2018).

3.2.3. Near-UV and Near-IR Spectra

A comparison of the near-UV spectra of SN 2017eaw with those of two other Type II-P SNe, 2012aw and 2013ej, is presented in Figure 10. Based on the findings of Gal-Yam et al. (2008), Type II-P SNe look very similar in the 2000–3000 Å range; however, there are only a few objects with high-quality data. In the left panel of Figure 10, we show the two near-UV spectra of SN 2017eaw together with the sequence of early-phase spectra of SN 2012aw (Bayless et al. 2013). All spectra are corrected for extinction and normalized to the same flux level between 4000 and 4500 Å. Note that the strong flux depression in the +10 day spectrum of SN 2017eaw is not real; it is due to contamination caused by the presence of zeroth-order images of nearby stars in the background region of the SN spectrum. Disregarding the contaminated region, the spectra of both SNe, as well as their evolution, are very similar, confirming the findings by Gal-Yam et al. (2008).

The right panel of Figure 10 contains the same two near-UV spectra of SN 2017eaw but compared to those of SN 2013ej (Dhungana et al. 2016). The similarity is less pronounced in this case, as SN 2017eaw appears to be relatively brighter than SN 2013ej between 2500 and 3500 Å at +10 days. As SN 2013ej was a “transitional” object between the Type II-P (“plateau”) and II-L (“linear”) SNe (Dhungana et al. 2016), such minor differences between the near-UV spectra are not unexpected and likely real.

Because all three SNe showed X-ray emission shortly after explosion (see Bayless et al. 2013; Chakraborti et al. 2016, as well as Section 4.2) that are consistent with the presence of very nearby CSM, the relatively lower near-UV flux of SN 2013ej is probably not due to the lack of early CSM interaction. As SN 2013ej showed a shorter plateau than 2017eaw in its optical LCs (Dhungana et al. 2016), a faster spectral evolution, i.e., a faster decline of the near-UV flux in time, may be a more likely cause of the difference of its near-UV spectra with those of SNe 2017eaw.

The five near-IR spectra of SN 2017eaw, obtained with IRTF between +6 and +39 days, are plotted in Figure 11. During the early phases, the spectra do not show many features; they are mostly dominated by the P Cygni profiles of the Ca II triplet and the hydrogen Paschen features. Nevertheless, the +6 and

+11 day IRTF spectra are the earliest near-IR spectra of SN 2017eaw published to date.

Moreover, the contemporaneous near-UV, optical, and near-IR spectra obtained at +10/11 days allowed us to make a well-constrained estimation of the photospheric temperature based on a wider wavelength range. We constructed a combined spectrum, which can be well fitted with a $T = 14,000$ K blackbody (see Figure 12); this value is in good agreement with the photospheric temperature determined by Bose et al. (2013) from the spectral modeling of SN 2012aw at the same epoch.

Based on higher-resolution spectra obtained with the Gemini Near-Infrared Spectrograph between +22 and +205 days, Rho et al. (2018) carried out a more detailed analysis of SN 2017eaw. Their most important conclusion is that the spectra show the formation of a moderate amount of CO molecules and hot dust after ~ 120 days. We will return to this finding in Section 4.3.

3.3. Distance Estimates

The distance to SN 2017eaw and its host galaxy is estimated by combining the results from various methods, as detailed below.

3.3.1. Expanding Photosphere Method

First, we apply the expanding photosphere method (EPM) to the combined data set of SN 2017eaw (this paper) and 2004et (Sahu et al. 2006; Misra et al. 2007; Maguire et al. 2010). The photospheric velocities are derived from the absorption minima of $H\beta$ and the standard Fe II $\lambda 5169$ feature, as shown in the previous section. For the explosion dates, we adopt JD 2,453,270.5 (Li et al. 2005) for SN 2004et and JD 2,457,886.5 for SN 2017eaw (see above).

Our method uses the combination of the LCs and velocity curves of two SNe that exploded within the same host galaxy. This technique has been applied for a number of cases recently: SN 2011dh and 2005cs in M51 (Vinkó et al. 2012) and SN 2013ej and 2002ap in M74 (Dhungana et al. 2016). The constraint that the distance must be the same for both SNe helps to overcome some of the issues related to the application of the EPM to a single object, e.g., the sensitivity to the explosion date or stronger deviations from the modified blackbody evolution.

After correcting for the interstellar extinction using $E(B - V)_{\text{tot}} = 0.41$ mag for the total reddening (see above) and assuming $R_V = 3.1$ for the extinction law, we construct a quasi-bolometric LC for both SNe from their measured $BVRI$ data (see Section 3.5). Then we fit the standard equations of the EPM (e.g., Vinkó et al. 2012) coupled with the dilution factors of Dessart & Hillier (2005) to the

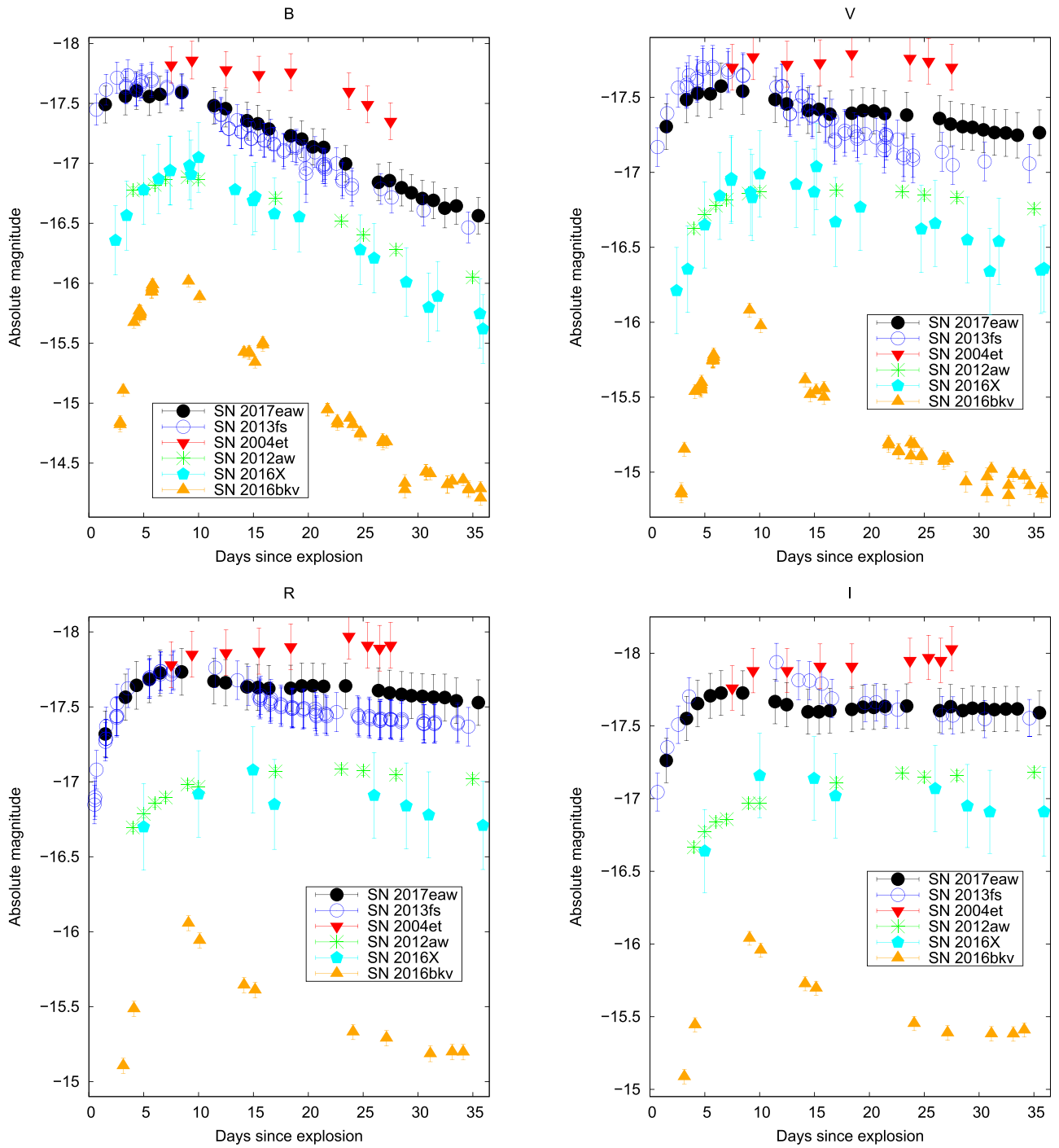


Figure 4. Early optical LCs of SN 2017eaw compared to those of other normal or interacting Type II-P SNe.

quasi-bolometric LCs simultaneously. The fit is restricted to the epochs $10 \text{ days} < t < 50 \text{ days}$ after explosion for several reasons. First, the LC of SN 2017eaw shows a bump at the earliest epochs (Figure 4) that might be due to physical processes (e.g., CSM interaction) that are not included in the simple physical model (an expanding blackbody) used in the EPM. Also, at $t < 10 \text{ days}$, the contribution from the *UV*-band flux, which is treated only approximately when assembling the quasi-bolometric LCs, is higher than at later phases. After $\sim 10 \text{ days}$, these complications seem to have less effect. After $t \sim 50 \text{ days}$, NLTE effects become increasingly dominant (see, e.g., Dessart & Hillier 2005), which also causes deviations

from the simple blackbody approximation used in the EPM. Thus, as a compromise, we fit the equations of the EPM to data taken at $10 \text{ days} < t < 50 \text{ days}$.

The result is shown in Figure 13. The slope of the line gives $D = 7.15 \pm 0.30$ (statistical) ± 0.70 (systematic) Mpc. The quoted systematic uncertainty comes from two main sources: a $\pm 1 \text{ day}$ uncertainty in the adopted explosion dates and the sensitivity of the distance to the minimum and maximum epochs used in the EPM fitting. If we restrict the fitting to data taken in $0 \text{ days} < t < 30 \text{ days}$, as recommended by Dessart & Hillier (2005), we get an $\sim 0.7 \text{ Mpc}$ higher common distance (see Table 2).

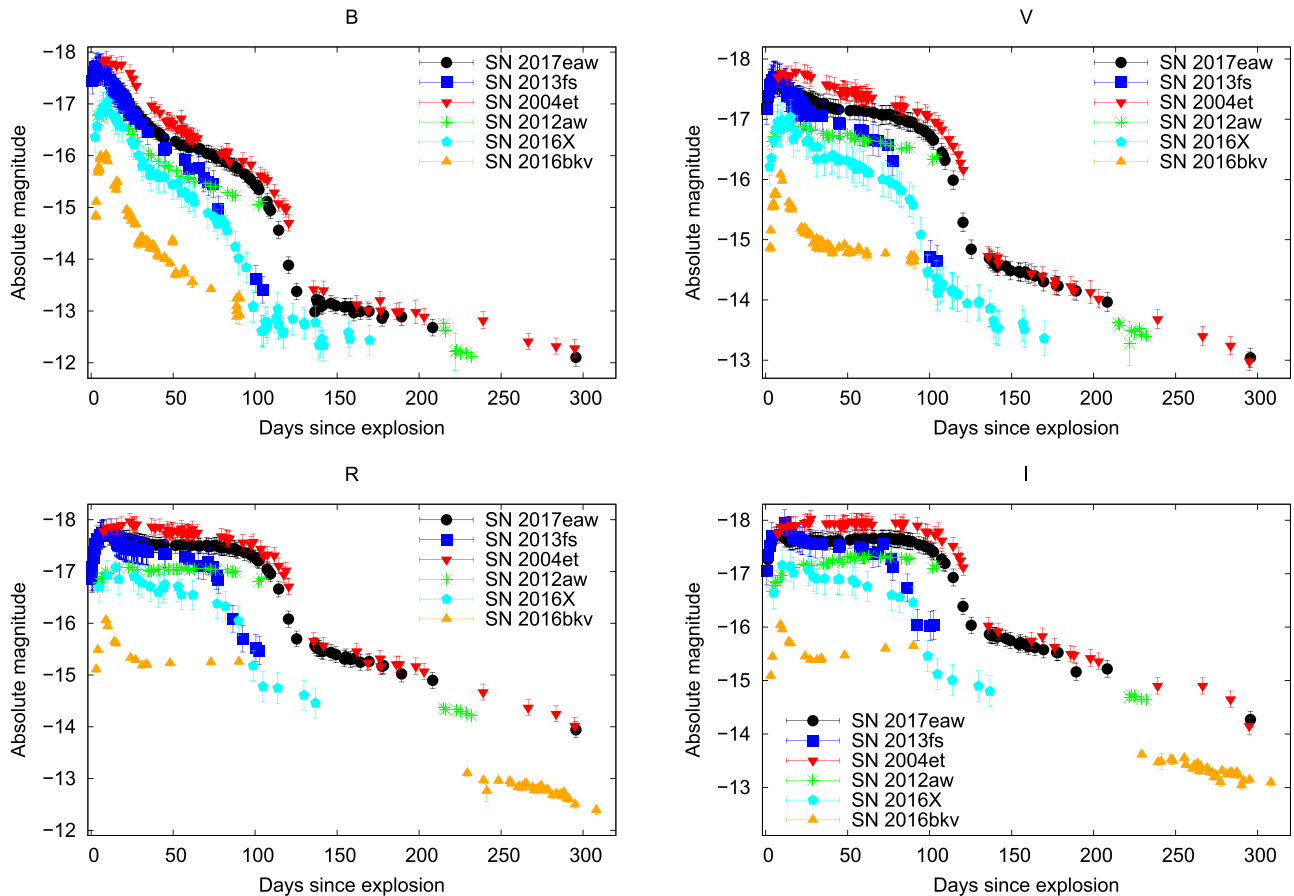


Figure 5. Full optical LCs of SN 2017eaw compared to those of other normal or interacting Type II-P SNe.

From Figure 13, it is seen that the data of the two SNe, even though they are consistent within the errors, start to deviate systematically from each other after $t > +30$ days. Thus, fitting the equations of the EPM to only one of them would give different distances. Indeed, fitting only to SN 2004et, but also letting the moment of explosion (t_0) float, would result in $D \sim 5.23 \pm 0.15$ Mpc and t_0 being ~ 5 days later than the assumed moment of explosion (see above), which is in conflict with the discovery date. Using SN 2017eaw only, the same analysis would give $D \sim 7.08 \pm 0.11$ Mpc and $t_0 \sim 1.9$ days later than assumed. These conflicting results illustrate why the fitting to the combined data set (coupled with the constraints on the moment of explosion) can give more reliable results. Keeping in mind the uncertainties of reddening/extinction and the explosion date, this might explain why the previous applications of EPM to SN 2004et resulted in lower ($D \sim 5$ Mpc) distances (see, e.g., Takáts & Vinkó 2012, and references therein).

Note that the application of the template velocity curve based on spectroscopic modeling by Takáts & Vinkó (2012) gives a distance that is only ~ 0.1 Mpc lower; thus, it is within the uncertainty of the fitting.

The results detailed above also depend on the assumed reddening ($E(B - V)_{\text{tot}} = 0.41$). If we adopt only the reddening from the Milky Way dust, $E(B - V) \sim 0.3$ (Schlafly & Finkbeiner 2011), and thus ignore the reddening within NGC 6946, then the EPM distance from the combined data set would decrease to $D \sim 6.7$ Mpc. Given that dust in the host galaxy should also contribute somewhat to the total reddening, this is probably a lower limit, and the true distance is closer to

~ 7 Mpc. Table 2 summarizes the distances derived above and from other methods (see below).

3.3.2. Standard Candle Method

Second, we estimate the distance to SN 2017eaw by applying the standard candle method (SCM). This method was first proposed by Hamuy & Pinto (2002), and it was refined and recalibrated in various later studies (Takáts & Vinkó 2006; Poznanski et al. 2009; D’Andrea et al. 2010; Maguire et al. 2010; Olivares et al. 2010; Gall et al. 2016; de Jaeger et al. 2017).

For SN 2017eaw, we measure $m_V(50) = 13.20$, $m_I(50) = 12.25$, $m_r(50) = 12.77$, $m_i(50) = 12.61$, $v_{\text{Fe II}}(50) = 4600 \pm 200$, and $v_{\text{H}\beta}(50) = 5350 \pm 200$ km s $^{-1}$ for the V-, I-, r-, and i-band magnitudes and expansion velocities at $t = 50$ days after explosion, respectively. Table 2 lists the distances of SN 2017eaw inferred from the three most recent SCM calibrations.

Compared to other distances listed in the NASA/IPAC Extragalactic Database (NED), most of which are based on using SCM on SN 2004et (~ 5 Mpc), these new SCM-based distances to SN 2017eaw are all systematically higher. This is the same as found above when comparing the individual EPM-based distances of SNe 2017eaw and 2004et. The lower SCM-based distance to SN 2004et is due to the fact that SN 2004et showed a brighter plateau but lower expansion velocity at $t = 50$ days than SN 2017eaw. Indeed, from the data by Sahu et al. (2006) and Maguire et al. (2010), we measure $m_V(50) = 12.83$, $m_I(50) = 11.93$, and $v_{\text{Fe II}}(50) = 4230 \pm 200$ km s $^{-1}$ and

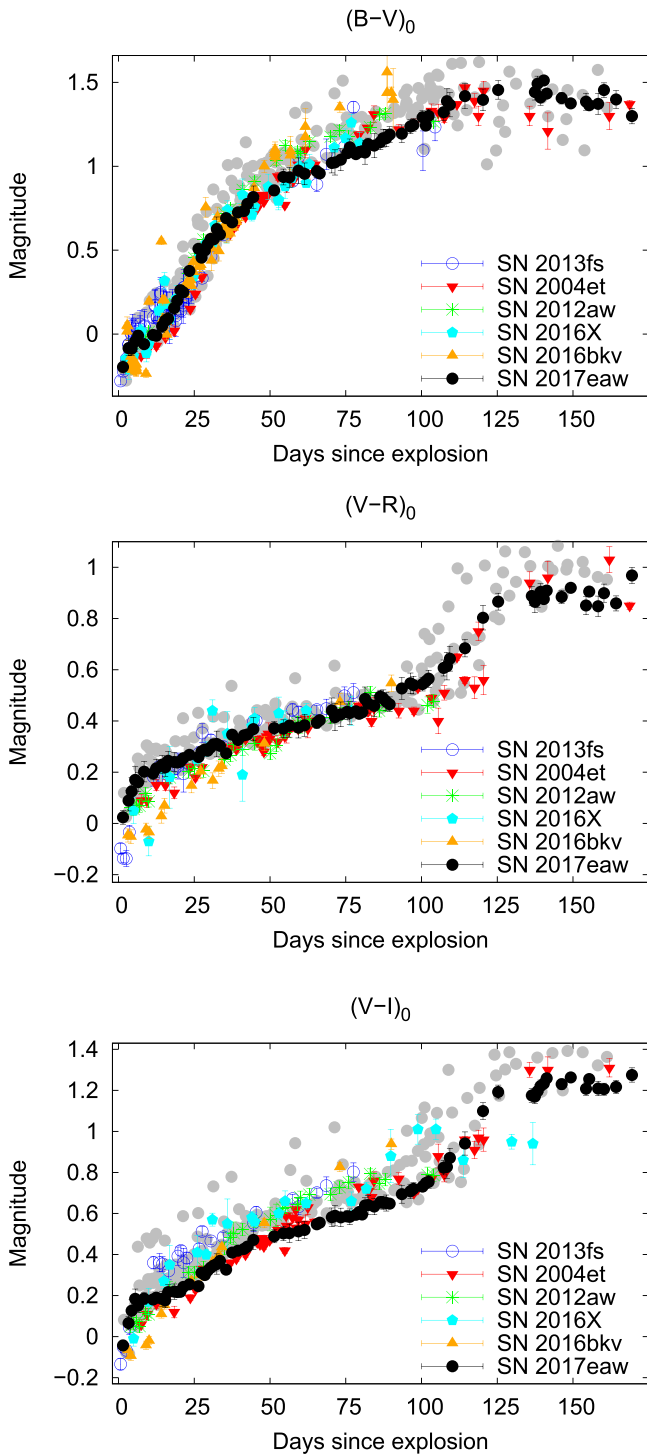


Figure 6. Dereddened color curves of SN 2017eaw compared to those of other normal or interacting Type II-P SNe. Data marked with colored symbols are adopted from sources given in Table 1, while all other data (gray circles) are from Faran et al. (2014).

derive $D = 5.43 \pm 0.24$ Mpc from the calibration by Poznanski et al. (2009). If we correct the plateau brightness for Milky Way extinction ($E(B - V) = 0.3$ mag) first and use these corrected magnitudes, then the SCM-based distance to SN 2004et decreases to $\sim 4.9 \pm 0.2$ Mpc. Overall, the SCM distances show the same trend as the EPM-based distances: they seem to be systematically higher for SN 2017eaw than for SN 2004et. This strengthens the suspicion that SN 2004et was not a typical Type II-P; thus, the

previous distance estimates based on SN 2004et are probably biased.

3.3.3. Other Distances to the Host Galaxy

The NED also contains other redshift-independent distance estimates for NGC 6946 that are not related to SN data. In Table 2, we list the four most recent ones that are based on the tip of the red giant branch (TRGB; Tikhonov 2014; Anand et al. 2018) and planetary nebula luminosity function (PNLF; Herrmann et al. 2008) methods. The PNLF distance ($D \sim 6$ Mpc) is between the ones derived for SN 2017eaw ($D \sim 7$ Mpc) and 2004et ($D \sim 5$ Mpc), while the other two are closer to that of SN 2017eaw.

We assign the average of the various distances listed in Table 2 to the final distance of NGC 6946, i.e., $D \sim 6.85 \pm 0.63$ Mpc (the quoted uncertainty is the rms error but takes into account the uncertainties of the individual distances). This value disfavors the previous measurements from SN 2004et that all gave $\sim 30\%$ lower distances. We use $D = 6.85$ Mpc as the distance to SN 2017eaw in the rest of this paper.

3.4. Progenitor Mass from Nebular Spectra

Observations taken during the nebular phase (~ 200 – 500 days post-explosion) reveal the inner nucleosynthetic products of the progenitor star and its explosive burning. The strength and shape of the emission lines of individual elements can be mapped back to the properties of the progenitor and explosion. In particular, a monotonic relation exists between the intensity of the [O I] doublet ($\lambda\lambda 6300, 6364$) and the mass of the progenitor star (Jerkstrand et al. 2012, 2014). We use this relationship to find the progenitor mass of SN 2017eaw using the spectra taken during the nebular phase.

We model the oxygen emission line using the suite of models presented in Jerkstrand et al. (2012), which are computed using the spectral synthesis code described in Jerkstrand et al. (2011). Model spectra are produced for $M_{\text{ZAMS}} = 12, 15, 19,$ and $25 M_{\odot}$ at epochs of 212, 250, 306, 400, and 451 days for the 12, 15, and $25 M_{\odot}$ models and at 212, 250, 332, 369, and 451 days for the $19 M_{\odot}$ model. These models were generated for SN 2004et using a nickel mass of $M_{\text{Ni,mod}}^{56} = 0.062 M_{\odot}$ and $d_{\text{mod}} = 5.5$ Mpc. To apply these models to SN 2017eaw, the synthetic spectra are scaled to the inferred distance and nickel mass of SN 2017eaw via the following relation:

$$F_{\text{obs}} = F_{\text{mod}} \times \left(\frac{d_{\text{mod}}}{d_{\text{obs}}} \right)^2 \left(\frac{M_{\text{Ni,obs}}^{56}}{M_{\text{Ni,mod}}^{56}} \right) e^{\frac{t_{\text{mod}} - t_{\text{obs}}}{111.4}}, \quad (1)$$

where F_{obs} and F_{mod} are the observed and model fluxes, d_{obs} and d_{mod} are the observed and model distances, and $M_{\text{Ni,obs}}^{56}$ and $M_{\text{Ni,mod}}^{56}$ are the observed and model nickel masses synthesized during the explosion. Although SNe 2004et and 2017eaw are in the same galaxy, we use the distance found in Section 3.3 as the distance to SN 2017eaw and scale the flux accordingly.

Using this method, we find the progenitor mass to be $15 M_{\odot}$ for the first nebular spectrum and $12 M_{\odot}$ for the two later spectra. However, we find that the blue part of the continuum in the last two observed spectra is noticeably below the continuum in the models. For this reason, we scale the models

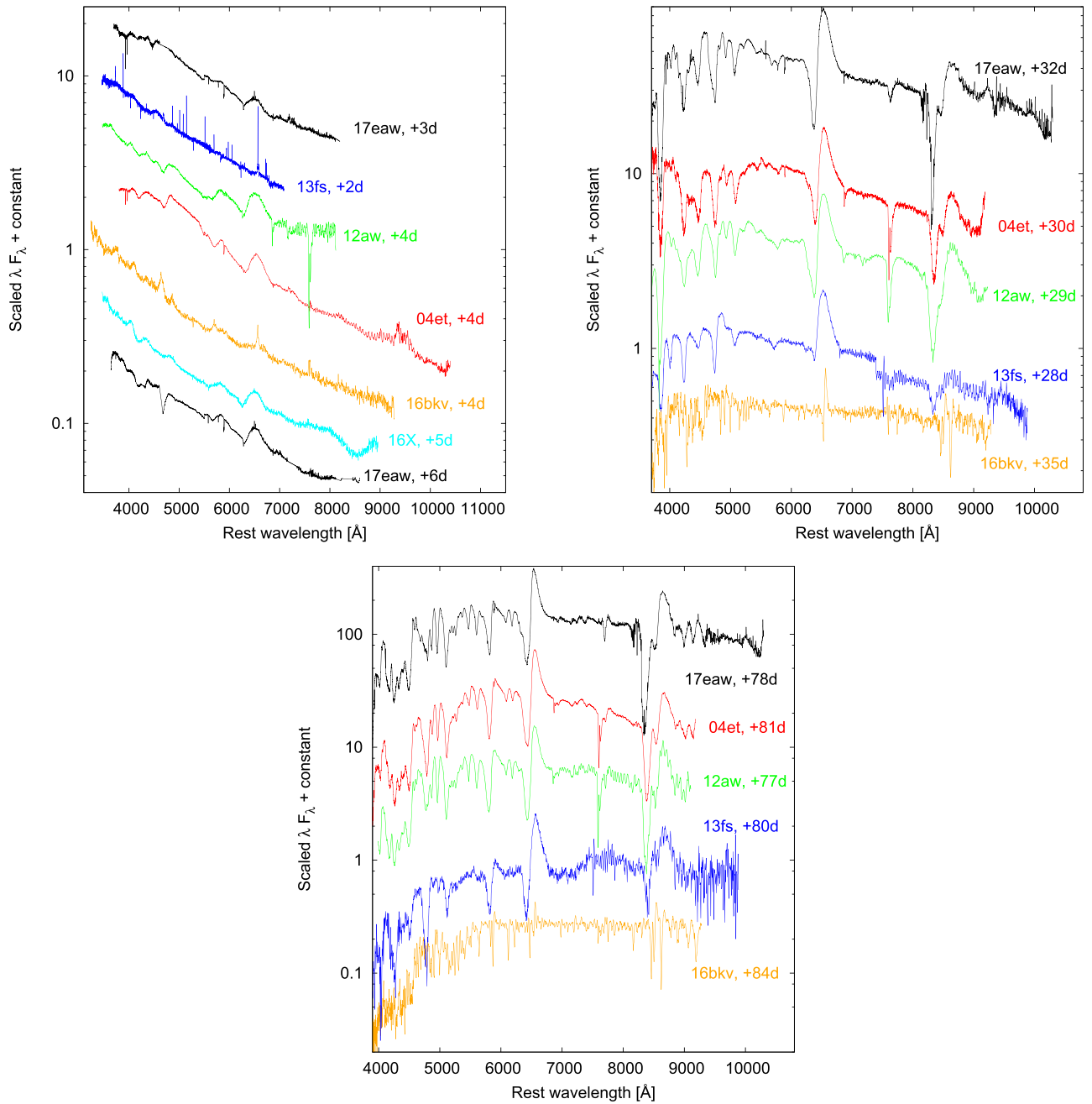


Figure 7. Optical spectra of SN 2017eaw compared to those of other normal or interacting Type II-P SNe. All spectra are corrected for redshift and extinction.

empirically by the ratio of the integrated flux of the observed and model spectra. This produces a much better alignment of the continuum on the blue side of the spectrum and a consistent progenitor mass of $\sim 15 M_{\odot}$ for all three spectra. The empirically scaled model spectra are plotted with the observed spectra in Figure 14. The inset in each panel shows the oxygen doublet in detail. As a sanity check, we use the empirical scale factor at each epoch and Equation (1) to compute the inferred nickel mass of SN 2017eaw. We find values of $0.025\text{--}0.036 M_{\odot}$ for the $15 M_{\odot}$ model, reasonably close to the value found in Section 3.5.

3.5. Modeling the Bolometric LC

The quasi-bolometric LC, including the contributions from the UV and IR, is constructed by applying the same technique

as described in Dhungana et al. (2016). After correcting the data for the total interstellar extinction (assuming $E(B - V) = 0.41$ mag; see Section 3) and converting the magnitudes to physical fluxes, the spectral energy distributions (SEDs) are integrated along the wavelength using the trapezoidal rule. Note that computing proper extinction correction for the *Swift* UV data is not as simple as for the optical data (Brown et al. 2010, 2016). Here we follow a somewhat simplified procedure by assuming constant extinction coefficients for the UVOT filters as determined by Brown et al. (2010) for the Type II-P SN 1999em (see their Table 14). The optical data are integrated between the *B* and *I* bands, while the *Swift* data are used to compute the contribution between the *B* band and 2000 \AA . The integrated flux from the unobserved IR bands is taken into account by extrapolating the

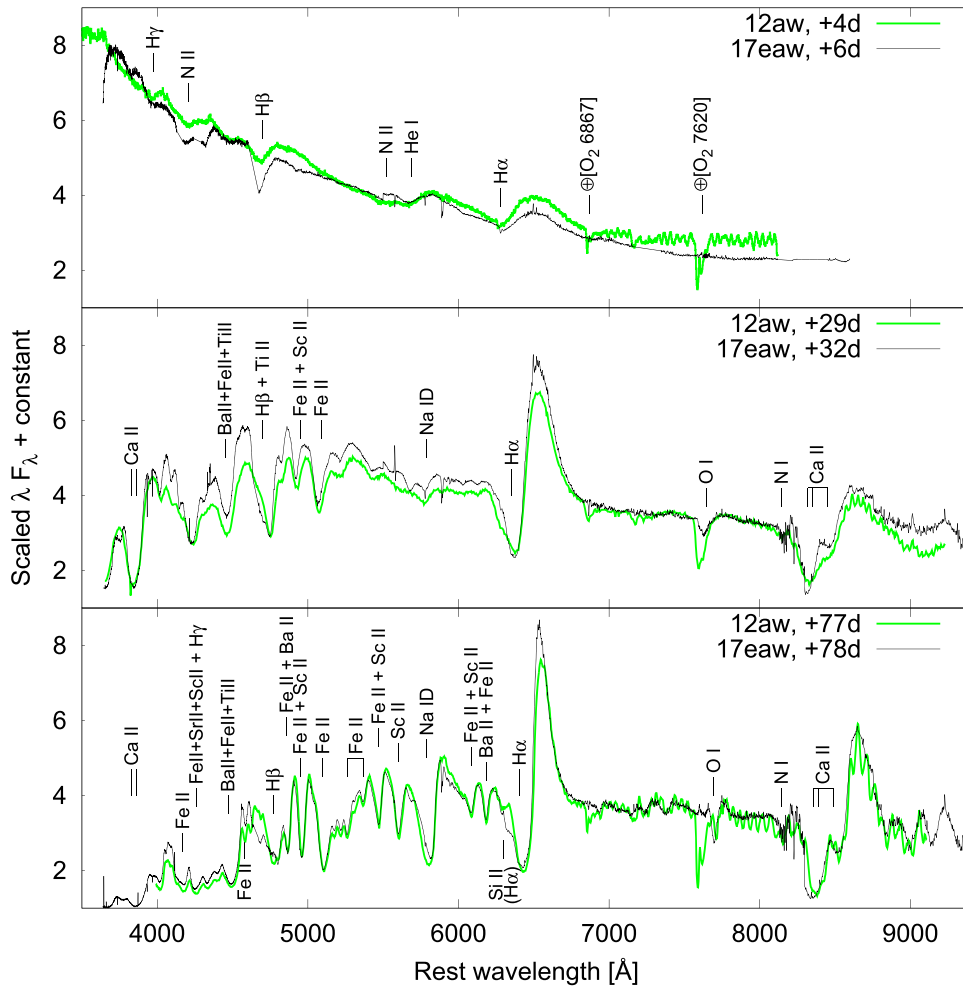


Figure 8. Line identification based on the SYNOW modeling of SN 2012aw (Bose et al. 2013). Note that at days +77/78, the small absorption component on the blue side of the H α P Cygni profile may be a high-velocity H feature instead of Si II 6355 Å; see Gutiérrez et al. (2017).

I-band fluxes with a Rayleigh–Jeans tail and integrating that curve to infinity. Finally, the integrated fluxes are corrected for distance using $D = 6.85$ Mpc (Section 3.3). The resulting quasi-bolometric LC is plotted, together with those of SNe 2012aw (Bose et al. 2013) and 2013ej (Dhungana et al. 2016) in Figure 15.

Radiation-diffusion models (Arnett & Fu 1989; Fu & Arnett 1989) for the bolometric LC are computed with the LC2.2 code²⁴ (Nagy & Vinkó 2016) that assumes a two-component ejecta having an inner, denser, more massive envelope (referred to as the “core,” following Nagy & Vinkó 2016) and an outer, less massive, lower-density “shell.” The code takes into account H or He recombination in the same way as in Arnett & Fu (1989). More details on the physics of these models can be found in Nagy & Vinkó (2016). Briefly, the main difference between the two components is that the outer, low-density shell is assumed to be powered only by shock heating (and not by ^{56}Ni decay).

The right panel of Figure 15 plots the observed bolometric LC together with several models that are found to show similar luminosity evolution. The model parameters are listed in Table 3: the progenitor radius R_0 (in 10^{13} cm units), the mass of the ejecta (M_{ej} , in M_{\odot}), the initial mass of the radioactive

^{56}Ni (M_{Ni} , in M_{\odot}), the total energy (E_{tot} , in 10^{51} erg) and the ratio of the thermal (E_{th}) and kinetic energy (E_{kin}) of the ejecta, the opacity (κ , in $\text{cm}^2 \text{g}^{-1}$), the scaling velocity (v_{sc} , in km s^{-1}), and the LC timescale (t_{lc} , in days) (the geometric mean of the expansion and diffusion timescales is defined by Arnett & Fu 1989). The last two parameters are derived from the previous ones listed above.

The density profiles for all models are assumed to be constant, as in Arnett & Fu (1989). The shell is assumed to be hydrogen-rich; thus, the usual $\kappa = 0.34 \text{ cm}^2 \text{g}^{-1}$ (which is equal to the Thompson-scattering opacity of a fully ionized solar-like plasma) is adopted as the opacity in this component. Since the core is more abundant in heavier elements, its Thompson-scattering opacity could be somewhat lower; thus, $\kappa \sim 0.24 \text{ cm}^2 \text{g}^{-1}$ is adopted there (Nagy 2018). For the recombination temperature, two different values ($T_{\text{ion}} = 5500$ and 7500 K) are assumed as lower and upper limits that roughly bracket the recombination temperature in a hydrogen-rich and hydrogen-depleted atmosphere, respectively.

It has to be noted that, as described in detail in Nagy & Vinkó (2016), the uncertainty of the explosion date can be a serious limitation during this modeling process; at the same time, the ± 1 day uncertainty in t_0 of SN 2017eaw (see Section 3) may cause only an $\sim 5\%$ relative error in the derived physical parameters. Moreover, the mass estimate

²⁴ <http://titan.physx.u-szeged.hu/~nagyaudi/LC2.2/>

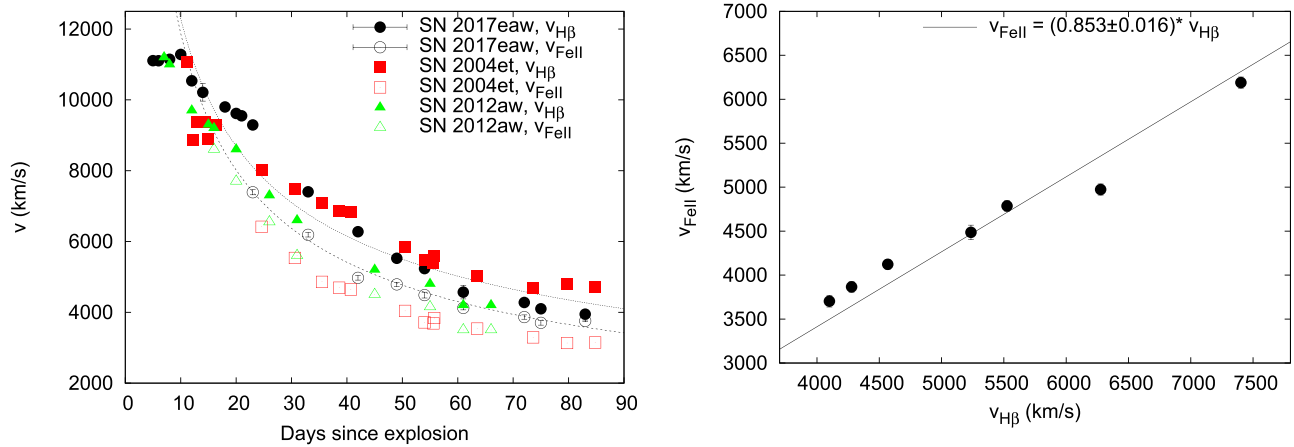


Figure 9. Left: velocity curves of SN 2017eaw compared to those of Type II-P SNe 2004et (Takács & Vinkó 2012) and 2012aw (Bose et al. 2013). Open and filled symbols denote velocities calculated from the Doppler shift of the absorption minima of the Fe II 5169 Å and H β lines, respectively. Dotted and dashed lines show the fitted curves of $v_{\text{Fe II}}(t)/v_{\text{Fe II}}(50) = (t/50)^{-0.567 \pm 0.021}$ and $v_{\text{H}\beta}(t)/v_{\text{H}\beta}(50) = (t/50)^{-0.499 \pm 0.020}$, respectively (see the text for details). Right: relation between the measured $v_{\text{Fe II}}$ and $v_{\text{H}\beta}$ values.

based on LC modeling has a well-known degeneracy with the assumed (constant) optical opacity and kinetic energy; these parameters are correlated via the t_{lc} parameter as $t_{\text{lc}} \sim \kappa M_{\text{ej}}^{3/2} E_{\text{kin}}^{-1/2}$. Thus, for the same LC but a slightly different opacity than in Table 3, one can get different ejecta masses. For example, if using $\kappa = 0.33 \text{ cm}^2 \text{ g}^{-1}$ in the core, one would get a factor of 0.8 lower mass, i.e., $M_{\text{ej}} \sim 11 M_{\odot}$. Therefore, a more realistic estimate for the uncertainty of the derived ejecta mass is at least $\pm 3 M_{\odot}$, which takes into account the correlation between these key parameters.

In Table 3, the parameters for SNe 2012aw and 2013ej calculated with the same two-component model (adopted from Nagy & Vinkó 2016) are also shown. While slightly different opacities have been used during the modeling of the three SNe, the main parameters are similar. This suggests that the three progenitors were probably similar to each other. However, as can also be seen in Figure 15, the early-time bolometric fluxes are larger in the case of SN 2017eaw, which can be modeled with a higher total energy in the core (or can be the sign of early-time CSM interaction). Further implications for the LC models are discussed in Section 4.

4. Discussion

From the observations and models presented in the previous sections, we draw a comprehensive picture of SN 2017eaw and its progenitor and circumstellar environment.

4.1. Mass of the Progenitor, Explosion Parameters

The model parameters shown in Table 3 imply a relatively, but not unusually, massive Type II-P SN ejecta: the total (core + shell) envelope mass is $\sim 14.5 \pm 3.0 M_{\odot}$. Assuming $\sim 1.4 M_{\odot}$ for the mass of the remaining neutron star, this is in good agreement with the progenitor mass of $\sim 15 M_{\odot}$ inferred from our modeling of the nebular spectra (during which we used 12, 15, 19, and 25 M_{\odot} models).

Tsvetkov et al. (2018) applied the multigroup radiation hydro code STELLA (Blinnikov et al. 1998, 2000, 2006) to model their *UBVRI* LCs for SN 2017eaw. They obtained $R_0 = 600 R_{\odot}$ ($\sim 4.2 \times 10^{13}$ cm), $M_{\text{ej}} = 23 M_{\odot}$, $M_{\text{Ni}} = 0.05 M_{\odot}$, and $E_{\text{kin}} = 2.0$ foe, which are consistent with our results in Table 3. The only exception is their ~ 1.5 times higher total

ejecta mass. It is a well-known issue that radiation hydro codes sometimes give higher envelope masses than simple semi-analytic models (e.g., Nagy & Vinkó 2016). Given the uncertainties of the parameters from the semi-analytic models, which use a lot of approximations, such a difference within a factor of 2 is not unexpected. Note that our derived mass is more consistent with the mass estimates for the observed progenitor of SN 2017eaw ($14 \pm 3 M_{\odot}$; van Dyk et al. 2017; Kilpatrick & Foley 2018), as well as with the results of Rho et al. (2018), who compared their near-IR spectra with the models of Dessart et al. (2017, 2018) and concluded a progenitor mass of $15 M_{\odot}$ (with M_{ej} of $12.5 M_{\odot}$ and M_{Ni} of $0.084 M_{\odot}$). Note also that Williams et al. (2018) gave a much lower value for the progenitor mass ($\sim 8.8_{-0.2}^{+2} M_{\odot}$) from modeling the local stellar population, but, from their Figure 2, this looks more like being a lower limit.

The initial shell radius of $\sim 4.5 \times 10^{13}$ cm is in very good agreement with the conclusion by Kilpatrick & Foley (2018) that the progenitor of SN 2017eaw was an RSG star.

4.2. Early-time Circumstellar Interaction, Mass Loss of the Progenitor

Being one of the nearest SNe in the last decade, SN 2017eaw has been intensively followed up in both the X-ray and radio bands in order to look for signs of possible early-time circumstellar interaction. Within only a day after discovery, the SN was positively detected in X-rays with the *Swift*/X-ray Telescope (XRT) at two different epochs, showing a significant early brightening in the 0.3–10 keV range by Kong & Li (2017), who also gave a (much lower) pre-explosion upper flux limit based on archival *Chandra* images of the SN site. A few days later, the SN was also observed with the *Nuclear Spectroscopic Telescope Array* (Grefenstette et al. 2017), detecting a slightly lower flux between 0.3 and 10 keV than previously found by *Swift*. Moreover, the latter authors also reported the presence of a line from ionized Fe around 6.65 keV, which implies the presence of shock-heated ejecta. Unfortunately, no further X-ray observations have been published to date; however, the SN has also been detected with the *AstroSat*/UV Imaging Telescope in the far-UV channel ~ 2 weeks after explosion (Misra et al. 2017).

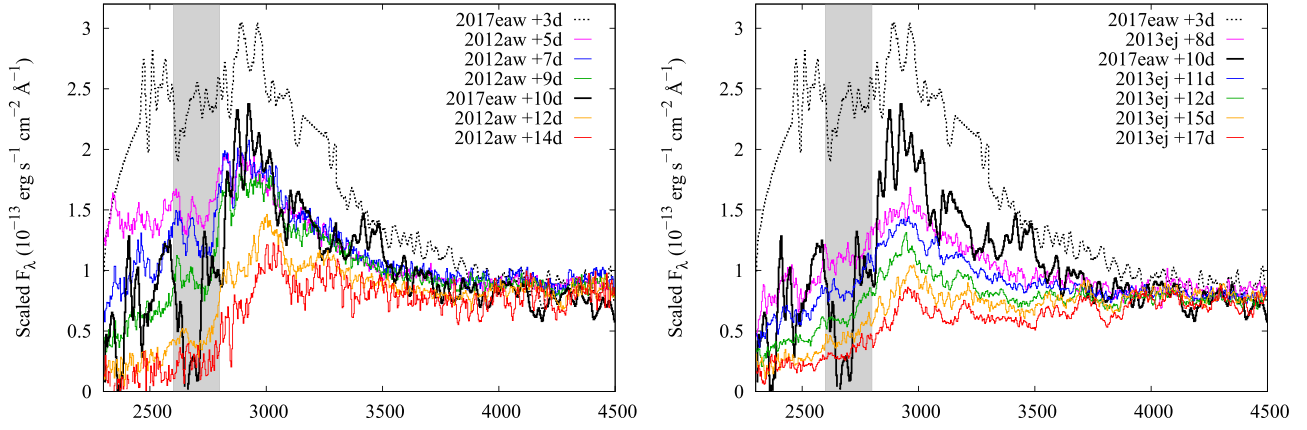


Figure 10. Early-phase near-UV spectra of SN 2017eaw taken with the *Swift* UVOT/UGRISM instrument (black curves) compared to those of SN 2012aw (Bayless et al. 2013; left panel) and SN 2013ej (Dhungana et al. 2016; right panel). All spectra are dereddened and normalized to the same flux level in the 4000–4500 Å regime. Note that the deep feature in the spectrum of SN 2017eaw at ~ 2700 Å (marked by gray shading) is artificial due to contamination of the background level from a nearby stellar source.

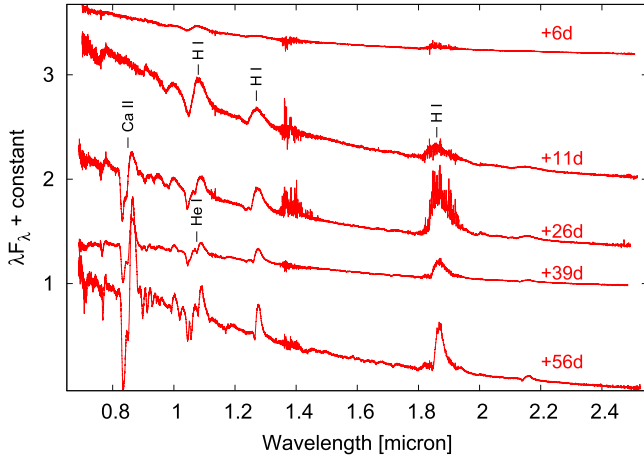


Figure 11. Near-IR spectra of SN 2017eaw obtained with NASA IRTF SpeX.

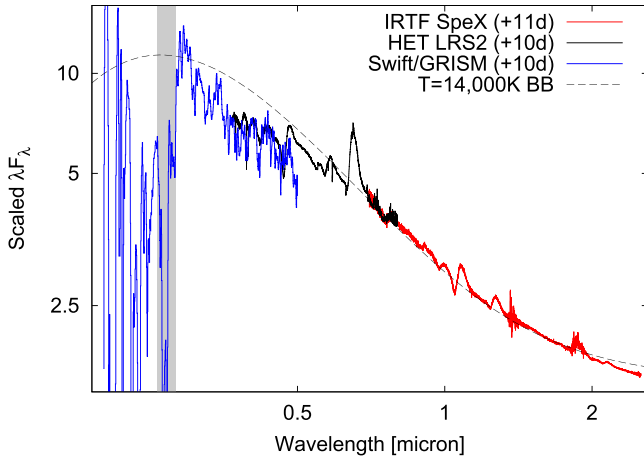


Figure 12. Simple fitting of a $T = 14,000$ K blackbody on a combined (near-UV–optical–near-IR) early-phase spectrum of SN 2017eaw. The contaminated region of the UV spectrum is marked by gray shading.

The top panel of Figure 16 presents all of the published X-ray fluxes measured for SN 2017eaw. Using the distance of $D = 6.85$ Mpc (see above), we determined the integrated unabsorbed X-ray luminosities for SN 2017eaw to be in the

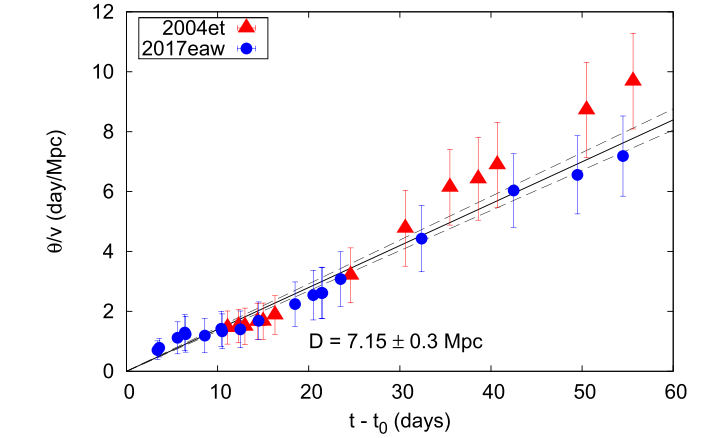


Figure 13. Distance determination from the EPM applied to the combined SN 2017eaw + 2004et data (see text). The slope of the solid line gives $\sim D^{-1}$, and the dashed lines illustrate the effect of a ± 0.3 Mpc statistical uncertainty in the distance.

Table 2
Distance Estimates to NGC 6946

Method	Calibration	$E(B - V)$	D (Mpc)	σ (Mpc)
EPM	A	0.41	7.15	0.3
EPM	A	0.30	6.66	0.3
EPM	B	0.41	7.85	0.2
EPM	B	0.30	6.93	0.4
SCM	C	...	6.69	0.3
SCM	D	...	6.69	0.2
SCM	E	...	6.02	0.3
TRGB	F	...	6.7	0.2
TRGB	G	...	7.7	0.3
PNLF	H	...	6.1	0.6
Average			6.85	0.63

Note. (A) 10 days $< t < 50$ days; (B) 10 days $< t < 30$ days; (C) Poznanski et al. (2009); (D) de Jaeger et al. (2017); (E) Gall et al. (2018); (F) Tikhonov (2014); (G) Anand et al. (2018); (H) Herrmann et al. (2008).

0.3–10 keV range as $L_X = 9.5 \times 10^{38}$, 29.5×10^{38} , and 27.9×10^{38} erg s $^{-1}$ at +1.5, +2, and +9 days, respectively.

In order to compare these X-ray luminosities with those of other Type II-P SNe, we have collected the available data from

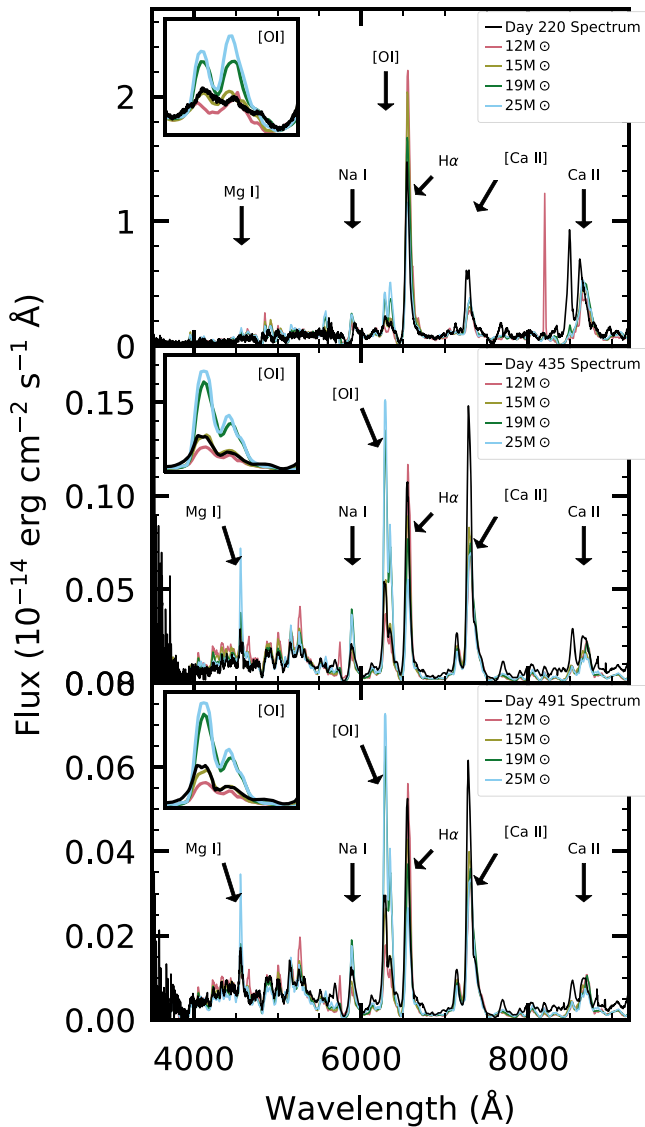


Figure 14. Nebular spectra of SN 2017eaw (black) observed 220 (top panel), 435 (middle panel), and 491 (bottom panel) days after explosion. The model spectra of Jerkstrand et al. (2012) are scaled by the integrated flux at each epoch such that the continua of the observed and model spectra are aligned for each 12 (pink), 15 (yellow), 19 (green), and 25 (blue) M_{\odot} progenitor. The [O I] line doublet ($\lambda\lambda 6300, 6364$) for the model and the observed spectra at each epoch is shown in the insets. The observed spectrum matches the 15 M_{\odot} model at all three epochs, implying that this is the M_{ZAMS} of the progenitor.

the literature. There are only a few SNe II-P that were observed in X-rays at such early phases. Figure 17 shows the X-ray luminosities (L_X) of SN 2017eaw, together with those of SNe 1999em (Pooley et al. 2002) and 2006bp (Immler et al. 2007) and the Type II-P/II-L 2013ej (Chakraborti et al. 2016) and 2016X (Grupe et al. 2016). It is seen that the L_X for SN 2017eaw (measured in the 0.3–10 keV range) is a few times higher than that of SNe 2006bp and 2016X and much higher than that of SNe 1999em and 2013ej (however, the latter objects were observed only in the 0.4/0.5–8 keV range). Note that if we use $D \sim 5$ Mpc for the distance of SN 2017eaw, we get $\sim 50\%$ lower L_X values, which are at the same level as that of SN 2006bp but still much larger than other published values regarding Type II-P SNe. We also

note that SN 2013fs was also followed up by *Swift*/XRT in the first ~ 25 days, and a combined upper limit of $L_X < 4.7 \times 10^{40}$ erg s $^{-1}$ was determined by Yaron et al. (2017); however, as those authors noted, most of the estimated flux may originate from the host galaxy instead of the SN, because of the relatively large distance.

While the level of early-time X-ray emission measured in SN 2017eaw is much lower than usually found in Type II or other strongly interacting SNe (see, e.g., Chevalier & Fransson 2017), its origin can be best explained by assuming a moderate interaction between the SN shock and the ambient circumstellar medium. As shown by, e.g., Immler et al. (2007) in the case of SN 2006bp, other possible sources (radioactive decay products of the ejecta or inverse Compton scattering of photospheric photons off relativistic electrons produced by the explosion) can be responsible for only a fraction of the observed X-ray emission.

Regarding radio observations, all of the early notifications reported nondetections at 1.4, 5.1, and 15 GHz (Argo et al. 2017a; Bright et al. 2017; Mooley et al. 2017; Nayana & Chandra 2017a). Later, subsequent observations at the two lower frequencies resulted in positive detections on three epochs: between +17 and 20 days at 5.1 GHz (using e-MERLIN; Argo et al. 2017b) and at +42 days at 1.4 GHz (using the Giant Metrewave Radio Telescope (GMRT); Nayana & Chandra 2017b). All of these data are shown in the middle panel of Figure 16. Since there are only a few observations of SN 2017eaw (obtained at three different frequencies), detailed modeling of the radio LCs cannot be accomplished. Nevertheless, the estimated radio luminosities at 5.1 GHz are $\sim 10^{26}$ erg s $^{-1}$ Hz $^{-1}$, which agree well with the peak luminosities of other Type II-P SNe assumed to go through moderate CSM interaction (see, e.g., Chevalier et al. 2006).

Beyond X-ray and radio data, optical LCs may also indicate the presence of early-time CSM interaction. As has been found by Moriya et al. (2011, 2017, 2018) and Morozova et al. (2017, 2018), the mass-loss processes of the presumed RSG progenitors may significantly affect the optical LCs of Type II(P) SNe, especially during the first few days. As mentioned in Section 3.1 and seen in Figure 4, SN 2017eaw shows a low-amplitude, early bump peaking at ~ 6 –7 days after explosion in the optical bands (most obviously in the *I* band and weakening toward shorter wavelengths). This phenomenon is quite similar to the one observed in SN 2013fs and is supposed to be caused by the interaction between the expanding SN ejecta and the ambient matter originating from the pre-explosion RSG wind.

There is a long-term debate over the amount, density distribution, and geometry of the circumstellar material surrounding SN progenitors, as well as the pre-explosion mass-loss history of RSG stars. In the basic (perhaps simplistic) framework, RSG stars have slow ($v_w \sim 10$ –20 km s $^{-1}$), steady winds resulting in mass-loss rates (\dot{M}) of 10^{-6} – $10^{-5} M_{\odot}$ yr $^{-1}$. At the same time, mass loss may become enhanced just before the explosion, resulting in a (more or less) compact and dense inner region in the CSM: $\dot{M} \sim 10^{-4}$ – $10^{-2} M_{\odot}$ yr $^{-1}$ and $R \sim 10^4 R_{\odot}$ (Moriya et al. 2011, 2017, 2018), or even $\dot{M} \sim 10^{-2}$ – $15 M_{\odot}$ yr $^{-1}$ and $R \sim 2000$ – $3000 R_{\odot}$ (Morozova et al. 2017, 2018). On the other hand, it is also possible that the shock simply breaks out from a very extended RSG atmosphere; in this case, the “superwind” description may not be adequate (see, e.g., Dessart et al. 2017).

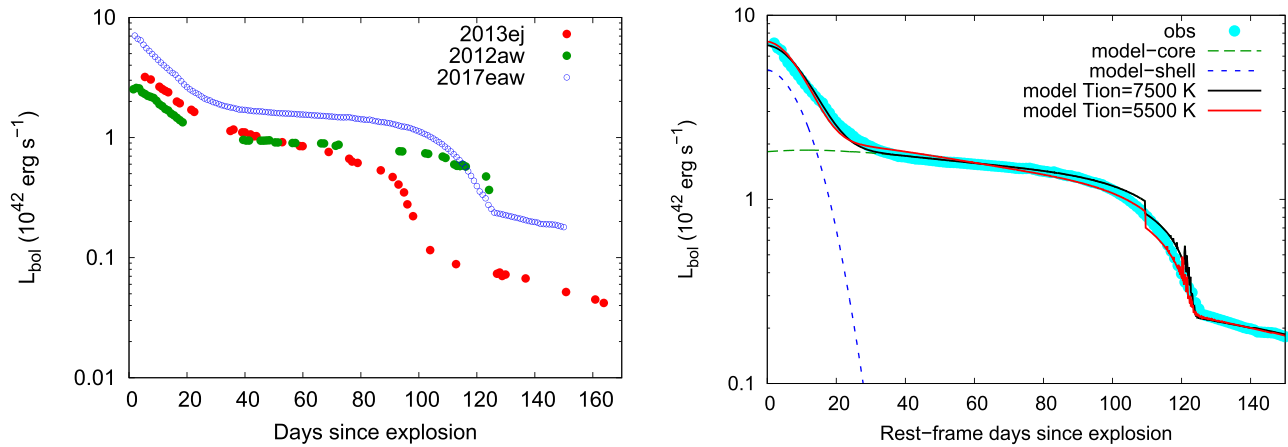


Figure 15. Left panel: bolometric LC of SN 2017eaw (including the UV contribution from *Swift*) compared to that of SNe 2012aw (Bose et al. 2013) and 2013ej (Dhungana et al. 2016). Right panel: fitting of two-component Arnett–Fu models (lines) to the bolometric LC of SN 2017eaw (circles). The contributions from the “core” and “shell” parts of the ejecta are plotted with long- and short-dashed lines, respectively. The kink in the model LCs at the end of the plateau phase is a numerical artifact related to the finite resolution of the grid used to locate the recombination front.

Table 3
Parameters of the Best-fit Two-component Arnett–Fu Models

T_{ion} (K)	SN 2017eaw		SN 2012aw	SN 2013ej
	7500	5500	7500	7500
Core				
R_0 (10^{13} cm)	3.3	2.0	2.9	2.9
M_{ej} (M_{\odot})	14.3	14.6	20.0	10.0
M_{Ni} (M_{\odot})	0.045	0.046	0.056	0.020
E_{tot} (10^{51} erg)	2.70	4.87	2.20	1.45
$E_{\text{kin}}/E_{\text{th}}$	1.99	1.92	2.67	3.14
κ ($\text{cm}^2 \text{g}^{-1}$)	0.24	0.24	0.13	0.20
v_{sc} (km s^{-1})	4583	6033	3660	4290
t_{lc} (days)	98.2	86.7	95.8	77.6
Shell				
R_0 (10^{13} cm)	4.9	4.5	4.5	6.8
M_{ej} (M_{\odot})	0.37	0.33	1.0	0.6
M_{Ni} (M_{\odot})
E_{tot} (10^{51} erg)	0.18	0.20	1.0	1.39
$E_{\text{kin}}/E_{\text{th}}$	1.93	2.22	9.0	14.4
κ ($\text{cm}^2 \text{g}^{-1}$)	0.34	0.34	0.40	0.40

Note. See the text for further explanation. Parameters for SNe 2012aw and 2013ej are adopted from Nagy & Vinkó (2016).

In the case of SN 2017eaw, Kilpatrick & Foley (2018) carried out a detailed investigation on the pre-explosion environment of the assumed progenitor using archived *HST* and *Spitzer* data (see above). They suggested the presence of a low-mass ($M > 2 \times 10^{-5} M_{\odot}$), extended ($R = 4000 R_{\odot}$) dust shell enshrouding the progenitor site. They also estimated the mass-loss rate by applying the method of Kochanek et al. (2012) and obtained $\dot{M} \sim 9 \times 10^{-7} M_{\odot} \text{ yr}^{-1}$.

Applying the method described in Kochanek et al. (2012; adopted from Chevalier & Fransson 2017) and using the parameters of our two LC models in Table 3 combined with the X-ray luminosities (L_{X}) given above, we can derive another constraint for \dot{M} via Equation (4) of Kochanek et al. (2012),

$$L_{\text{X}} \simeq 1.63 \times 10^7 E_{51}^{27/20} M_{e10}^{-21/20} \dot{M}_{-4}^{7/10} v_{w10}^{-7/10} \times t_1^{-3/10} L_{\odot}, \quad (2)$$

where the total energy of the SN is $E = 10^{51} E_{51}$ erg, the ejected mass is $M_{\text{ej}} = 10 M_{e10} M_{\odot}$, $\dot{M} = 10^{-4} \dot{M}_{-4} M_{\odot} \text{ yr}^{-1}$, $v_w = 10 v_{w10} \text{ km s}^{-1}$, and t_1 is the elapsed time in days (+5 and +9 days in this case).

Assuming $v_{w1} = 10 \text{ km s}^{-1}$ for the RSG wind velocity, we get $\dot{M} \sim 3 \times 10^{-7}$ and $\sim 1 \times 10^{-6} M_{\odot} \text{ yr}^{-1}$ for the two models listed in Table 3. Both of these values are consistent with the mass-loss rate estimated by Kilpatrick & Foley (2018). On the other hand, they are orders of magnitude lower than the mass-loss rates estimated by Moriya et al. and Morozova et al. via LC modeling or the value of $\dot{M} \sim 10^{-3} M_{\odot} \text{ yr}^{-1}$ derived by Yaron et al. (2017) for SN 2013fs based on modeling the early-time spectroscopic emission features. We note that from Equation (2), it would be necessary to have $L_{\text{X}} \sim 10^{41} \text{ erg s}^{-1}$ to get $\dot{M} \sim 10^{-3} M_{\odot} \text{ yr}^{-1}$ for the mass-loss rate of SN 2017eaw. Such high-level X-ray luminosity has been measured only in strongly interacting SNe II-n to date.

Nevertheless, while it seems to be a serious contradiction, some caveats in the above analysis must be mentioned. First, the mass-loss rate we estimated from X-ray luminosities (beyond the intrinsic uncertainties of the model) is based on the assumption that the dominating counterpart of L_{X} is the cooling of the reverse shock, and its softer emission dominates the observable X-ray flux; however, as Grefenstette et al. (2017) noted, the analysis of the +9 day X-ray spectrum of SN 2017eaw indicates a hard X-ray spectrum having detectable flux up to 30 keV (they also mentioned that the contribution of the 10–30 keV counterpart to the total L_{X} is $< 10\%$). Second, the radius of the dust-rich pre-explosion region ($\sim 4000 R_{\odot}$) derived by Kilpatrick & Foley (2018) is in good agreement with the general estimation given by Morozova et al. (2017, 2018) for the size of the cocoons of CSM around SNe II-P; the only difference is that the latter authors suggested the presence of a much denser environment. Signs of such a dense gas/dust shell are not seen in the combined optical-IR SED of the assumed progenitor of SN 2017eaw. High-resolution near-IR spectroscopy also did not detect narrow lines that may be an indication of CSM gas (see Rho et al. 2018). However, it is also true that these data do not cover the region of cold ($T \lesssim 300 \text{ K}$) dust. Third, a common problem is the geometry; while the models generally assume a spherically symmetric CSM, it may also take the form of a thick disk or a more complex structure

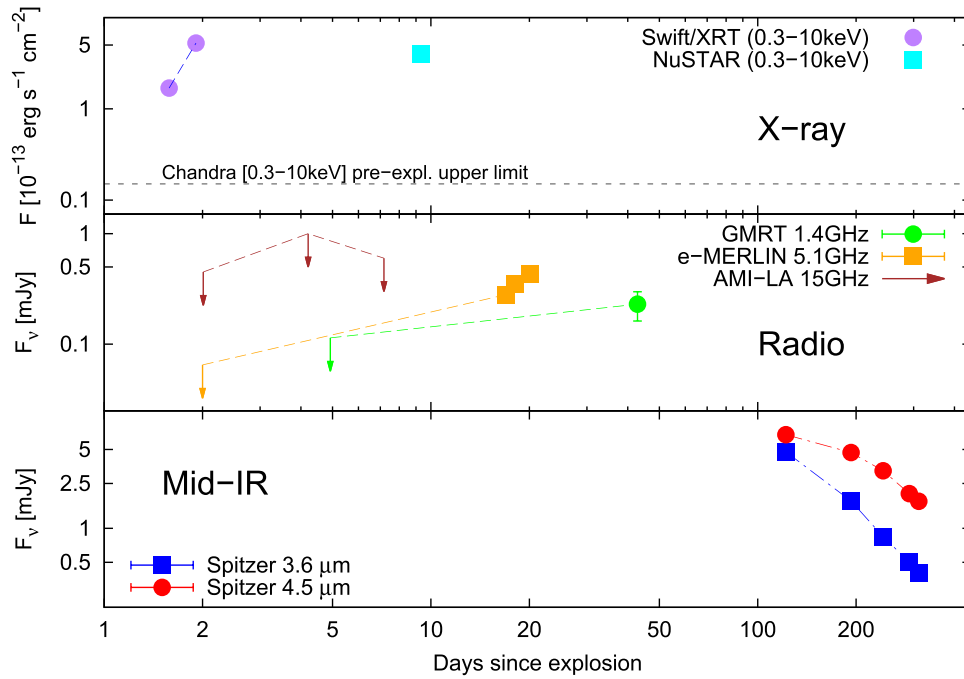


Figure 16. X-ray, radio and mid-IR data (together with published nondetections) of SN 2017eaw. Sources of data are listed in the text.

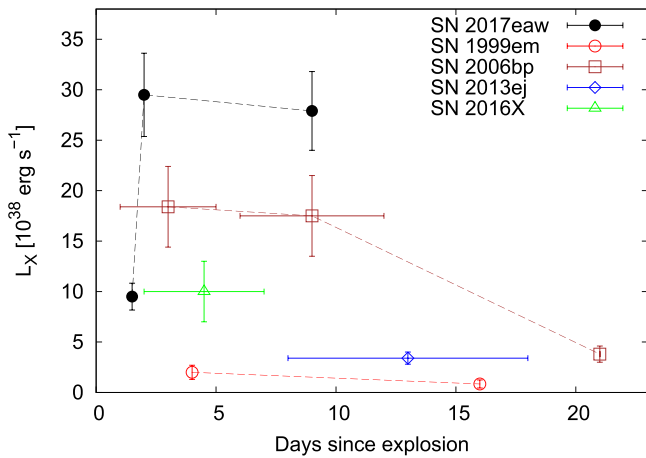


Figure 17. Early-time X-ray luminosities measured in Type II-P SNe: 2017eaw (0.3–10 keV), 1999em (0.4–8 keV, assuming a distance of $D = 12.5$ Mpc; Pooley et al. 2002), 2006bp (0.4–8 keV, assuming a distance of $D = 14.9$ Mpc; Immler et al. 2007), SN II-P/II-L 2013ej (0.5–8 keV, assuming a distance of $D = 9.57$ Mpc; Chakraborti et al. 2016), and 2016X (0.3–10 keV; Grupe et al. 2016). For the latter three objects, horizontal error bars indicate the (noncontiguous) periods covered by the observations.

of the inflated RSG envelope material (see, e.g., Dessart et al. 2017; Morozova et al. 2017, and references therein). The actual shape of the CSM cloud may also have a strong influence on the estimated parameters. All of these uncertainties point toward the need for further observations and more detailed modeling in order to better understand the role of nearby CSM around Type II-P SNe, as well as the mass-loss history of their RSG progenitors.

Moreover, it is also an intriguing question as to why we did not see any narrow (“flash-ionized”) emission lines in the earliest spectra of SN 2017eaw, unlike in the early (<5 days) spectra of SN 2013fs and several other interacting Type II SNe (Quimby et al. 2006; Khazov et al. 2016; Yaron et al. 2017). While this problem also requires further data and modeling, the

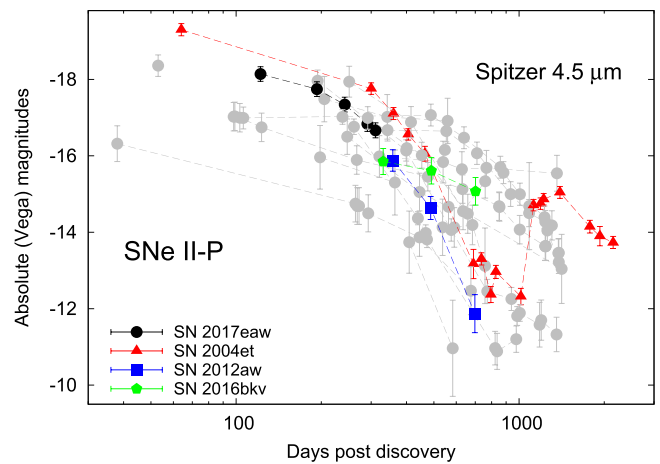


Figure 18. Mid-IR evolution of SN 2017eaw compared to that of other normal (gray) or interacting Type II-P SNe. The $4.5 \mu\text{m}$ magnitudes of SNe 2017eaw and 2016bkv come from this work, while the source of the other values is Szalai et al. (2018).

geometry and/or clumpiness of the CSM may also play a role here.

4.3. Possible Signs of Late-time Dust Formation

Using *Spitzer*, SN 2017eaw was also followed as the target of two different programs (PID 13239, PI: K. Krafton; PID 13053/SPIRITS, PI: M. Kasliwal). We have downloaded the public data from the *Spitzer* Heritage Archive (SHA)²⁵ and carried out simple aperture photometry on post-basic calibrated (PBCD) images. The SN appears as a bright, continuously fading object in both IRAC 3.6 and $4.5 \mu\text{m}$ channels. We present the results from our photometry in the bottom panel of Figure 16, while Figure 18 shows the $4.5 \mu\text{m}$ LC of SN 2017eaw compared to those of other Type II-P SNe (most

²⁵ <http://sha.ipac.caltech.edu>

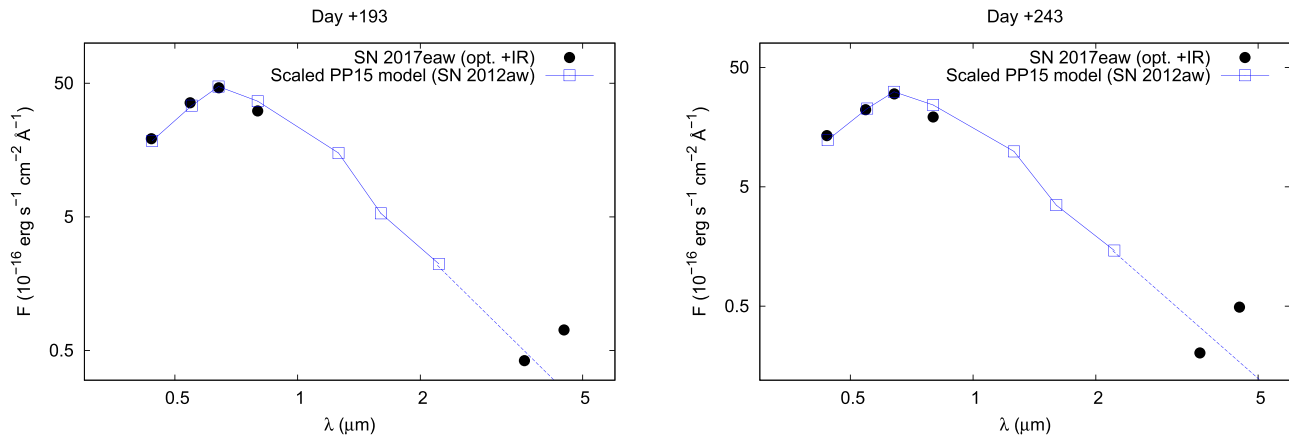


Figure 19. Optical-IR combined SED of SN 2017eaw (filled circles) compared to the scaled model SEDs of SN 2012aw calculated from Pejcha & Prieto (2015; PP15) (open squares).

of these data are adopted from Szalai et al. 2018, and references therein, while for SN 2016bkv, we carried out a similar process as above).

During the observed period, the mid-IR evolution of SN 2017eaw seems to be similar to that of the highlighted Type II-P events (SNe 2004et, 2012aw, and 2016bkv) that do not show strong, direct signs of dust formation (e.g., rebrightening in the mid-IR after several hundred days). At the same time, comparing the combined optical-IR SEDs of SN 2017eaw taken at +193 and +243 days (Figure 19) to model SEDs of SN 2012aw (Pejcha & Prieto 2015), there is a clear mid-IR excess in the $4.5 \mu\text{m}$ channel on both epochs. Here we note that in Type II-P SNe, the $4.5 \mu\text{m}$ flux may also be contaminated by the $1-0$ vibrational band of CO at $4.65 \mu\text{m}$, which can influence the SED modeling at epochs $\lesssim 500$ days (see, e.g., Kotak et al. 2005; Szalai et al. 2011).

These results seem to strengthen those of Rho et al. (2018), who, based on the detailed analysis of ground-based near-IR spectra, suggest ongoing (moderate) molecule (CO) and dust formation between ~ 125 and 205 days. A more detailed study of dust and molecule formation in SN 2017eaw was very recently published by Tinyanont et al. (2019); based on the analysis of the full *Spitzer* data set and near-IR photometry and spectroscopy up to ~ 550 days, these authors present similar conclusions to ours. We also note that, as can be seen, e.g., in the case of SN 2004et in Figure 18, dust formation can become more significant at later times ($\sim 800-1000$ days after explosion), probably due to an interaction between the forward shock and a denser CSM shell (see, e.g., Szalai et al. 2018, and references therein).

5. Conclusions

One of the most nearby SNe to appear in this decade, SN 2017eaw is a Type II-P explosion that shows early-time, moderate CSM interaction. We made a comprehensive study of this SN using multicolor optical photometry and high-quality optical spectroscopy starting at very early epochs and extending into the early nebular phase, near-UV and near-IR spectra, early-time X-ray and radio detections, and late-time mid-IR photometry.

We derived a new distance to the host galaxy, NGC 6946, after combining various distance estimates, including the EPM analysis of the combined data of SNe 2017eaw and 2004et.

The final distance, $D \sim 6.85 \pm 0.63$ Mpc, disfavors the previous measurements from SN 2004et that all gave $\sim 30\%$ lower distances.

During the whole period covered by the observations, the evolution of SN 2017eaw seems to be similar to that of some other “normal” Type II-P SNe (2004et, 2012aw). However, SN 2017eaw shows a small, early bump peaking at $\sim 6-7$ days after explosion in all optical bands, which resembles the early LC of SN 2013fs and is presumably a sign of early-time circumstellar interaction. Nevertheless, it is an intriguing question as to why we did not see any narrow (“flash-ionized”) emission features in the earliest optical spectra of SN 2017eaw; the solution to this problem might be related to different geometries and/or clumpiness of CSM around the two objects.

We modeled the quasi-bolometric LC of SN 2017eaw using a two-component radiation-diffusion model and estimated the basic physical parameters of the explosion and ejecta. We also carried out modeling of the nebular spectra using different progenitor masses. The results agree well with the previous findings of an RSG progenitor star with a mass of $\sim 15-16 M_{\odot}$.

We also used these calculated explosion parameters—together with early-phase X-ray luminosities—to derive the mass-loss rate of the progenitor. We got $\dot{M} \sim 3 \times 10^{-7} - 1 \times 10^{-6} M_{\odot} \text{ yr}^{-1}$; these values agree well with those estimated by Kilpatrick & Foley (2018) based on the opacity of the dust shell enshrouding the progenitor, but they are orders of magnitude lower than the generally estimated values for Type II-P SNe from early-phase LC modeling (Moriya et al. 2011, 2017, 2018; Morozova et al. 2017, 2018). We discussed several factors that may seriously influence the various estimations of \dot{M} , including the limitations within the models, as well as the simplifying assumptions on the geometry and clumpiness of the nearby CSM.

Finally, we also studied the available mid-IR data of SN 2017eaw. The combined optical-IR SEDs show a clear mid-IR excess at +193 and +243 days, which is consistent with the results of Rho et al. (2018) and Tinyanont et al. (2019) on the (moderate) dust formation in the vicinity of this SN.

We are thankful for the thorough work of an anonymous referee that helped us in improving this paper. This work is part of the project Transient Astrophysical Objects GINOP-2-3-2-15-2016-00033 of the National Research, Development and Innovation Office (NKFIH), Hungary, funded by the European

Union, and supported by the NKFIH/OTKA Grants K-109276, K-113117, and K-115709, the Lendület program of the Hungarian Academy of Sciences, project No. LP2018-7/2018, the ESA PECS Contract No. 4000110889/14/NL/NDe, and the New National Excellence, and the New National Excellence Program (UNKP-17-4) of the Ministry of Human Capacities of Hungary. T.S. has received funding from the Hungarian NKFIH/OTKA PD-112325 Grant. K.V. is supported by the Bolyai János Research Scholarship of the Hungarian Academy of Sciences. Research by D.J.S. is supported by NSF grants AST-1821967, 1821987, 1813708, and 1813466. J.C.W. is supported in part by NSF grant 1813825. The work of O.P. has been supported by the PRIMUS/SCI/17 award from Charles University in Prague. E.Y.H., C.A., and M.S. acknowledge the support provided by the National Science Foundation under grant No. AST-1613472. This work makes use of observations from the Las Cumbres Observatory network. D.A.H., G.H., and C.M. are supported by NSF grant AST-1313484. M.S., E.Y.H., and D.J.S. are visiting astronomers at the Infrared Telescope Facility, which is operated by the University of Hawaii under contract NNH14CK55B with the National Aeronautics and Space Administration. X.W. is supported by the National Natural Science Foundation of China (NSFC grants 11325313, 11633002, and 11761141001) and the National Program on Key Research and Development Project (grant 2016YFA0400803). Some of the data presented herein were obtained at the W. M. Keck Observatory, which is operated as a scientific partnership among the California Institute of Technology, the University of California, and the National Aeronautics and Space Administration. The Observatory was made possible by the generous financial support of the W. M. Keck Foundation. The authors wish to recognize and

acknowledge the very significant cultural role and reverence that the summit of Maunakea has always had within the indigenous Hawaiian community. We are most fortunate to have the opportunity to conduct observations from this mountain. This work is based on observations obtained at the Gemini Observatory (processed using the Gemini IRAF package), which is operated by the Association of Universities for Research in Astronomy, Inc., under a cooperative agreement with the NSF on behalf of the Gemini partnership: the National Science Foundation (United States), National Research Council (Canada), CONICYT (Chile), Ministerio de Ciencia, Tecnología e Innovación Productiva (Argentina), Ministério da Ciência, Tecnologia e Inovação (Brazil), and Korea Astronomy and Space Science Institute (Republic of Korea).

Facilities: LCO (1 m, 2 m), IRTF (SpeX), Konkoly (Schmidt), W. M. Keck Observatory (Keck I LRIS), Gemini Observatory (Gemini North GMOS), *Swift* (UVOT and XRT), *Spitzer* (IRAC).

Software: *astropy* (Astropy Collaboration et al. 2013), IRAF, HEASoft, SExtractor (Bertin & Arnouts 1996), Spextool (Cushing et al. 2004), XTELLCOR (Vacca et al. 2003), *lcofnpipe* (Valenti et al. 2016).

Appendix Photometric and Spectroscopic Data

Here we present the results of our Konkoly BVRI (in Vega-magnitudes, Table 4), LCO UVB $g'r'i'$ (in Vega-magnitudes for UVB and AB-magnitudes for $g'r'i'$ bands, Table 5) and *Swift* photometry (in Vega-magnitudes, Table 6). The journal of all spectroscopic observations is given in Table 7.

Table 4
Konkoly BVRI Photometry of SN 2017eaw

Date (MJD)	Epoch (days)	B (mag)	σ_B (mag)	V (mag)	σ_V (mag)	R (mag)	σ_R (mag)	I (mag)	σ_I (mag)
57,887.99	1.99	13.270	0.028	13.066	0.022	12.812	0.016	12.629	0.013
57,889.83	3.83	13.202	0.032	12.886	0.031	12.567	0.026	12.340	0.012
57,890.84	4.84	13.156	0.030	12.843	0.026	12.488	0.047	12.237	0.048
57,892.00	6.00	13.204	0.045	12.848	0.040	12.448	0.033	12.184	0.026
57,892.98	6.98	13.186	0.022	12.796	0.024	12.405	0.028	12.165	0.023
57,894.95	8.95	13.170	0.014	12.830	0.021	12.398	0.034	12.165	0.019
57,897.90	11.90	13.280	0.018	12.885	0.019	12.460	0.016	12.224	0.017
57,898.96	12.96	13.305	0.021	12.915	0.021	12.470	0.028	12.245	0.016
57,900.90	14.90	13.405	0.026	12.957	0.026	12.490	0.024	12.294	0.025
57,901.90	15.90	13.431	0.026	12.951	0.026	12.502	0.024	12.294	0.025
57,902.90	16.90	13.475	0.026	12.983	0.026	12.508	0.025	12.286	0.025
57,904.90	18.90	13.531	0.028	12.976	0.027	12.507	0.025	12.277	0.026
57,905.90	19.90	13.559	0.007	12.959	0.006	12.491	0.005	12.262	0.005
57,906.90	20.90	13.623	0.006	12.962	0.006	12.490	0.004	12.263	0.005
57,907.90	21.90	13.628	0.008	12.979	0.007	12.494	0.005	12.257	0.005
57,909.90	23.90	13.765	0.008	12.989	0.007	12.491	0.005	12.254	0.006
57,912.90	26.90	13.919	0.010	13.011	0.007	12.522	0.005	12.286	0.006
57,913.90	27.90	13.905	0.010	13.049	0.007	12.538	0.005	12.258	0.005
57,915.00	29.00	13.964	0.008	13.066	0.006	12.547	0.005	12.286	0.005
57,915.90	29.90	14.006	0.008	13.071	0.006	12.557	0.005	12.269	0.005
57,916.90	30.90	14.054	0.011	13.087	0.008	12.561	0.006	12.272	0.006
57,917.90	31.90	14.070	0.009	13.105	0.007	12.566	0.005	12.279	0.005
57,918.94	32.94	14.135	0.063	13.109	0.035	12.569	0.036	12.275	0.035
57,919.99	33.99	14.116	0.008	13.123	0.006	12.590	0.004	12.274	0.005
57,922.00	36.00	14.197	0.011	13.106	0.010	12.603	0.007	12.300	0.008
57,924.00	38.00	14.252	0.008	13.187	0.006	12.610	0.005	12.297	0.005

Table 4
(Continued)

Date (MJD)	Epoch (days)	B (mag)	σB (mag)	V (mag)	σV (mag)	R (mag)	σR (mag)	I (mag)	σI (mag)
57,925.95	39.95	14.301	0.010	13.176	0.006	12.620	0.005	12.277	0.005
57,927.90	41.90	14.327	0.009	13.194	0.008	12.620	0.005	12.286	0.006
57,929.02	43.02	14.375	0.010	13.199	0.007	12.622	0.005	12.281	0.005
57,931.00	45.00	14.425	0.054	13.209	0.039	12.611	0.022	12.258	0.024
57,937.86	51.86	14.486	0.023	13.230	0.022	12.628	0.015	12.261	0.023
57,940.90	54.90	14.558	0.038	13.222	0.028	12.622	0.020	12.239	0.020
57,942.91	56.91	14.563	0.044	13.229	0.039	12.617	0.023	12.245	0.021
57,945.90	59.90	14.605	0.070	13.231	0.030	12.627	0.027	12.238	0.034
57,947.90	61.90	14.595	0.059	13.240	0.027	12.627	0.033	12.240	0.031
57,951.92	65.92	14.632	0.030	13.262	0.020	12.638	0.010	12.235	0.010
57,952.90	66.90	14.627	0.010	13.270	0.007	12.637	0.005	12.235	0.005
57,956.90	70.90	14.717	0.046	13.297	0.038	12.626	0.031	12.235	0.024
57,957.94	71.94	14.723	0.063	13.300	0.041	12.655	0.034	12.231	0.028
57,959.87	73.87	14.738	0.055	13.299	0.035	12.643	0.033	12.238	0.028
57,961.96	75.96	14.770	0.023	13.292	0.020	12.626	0.023	12.226	0.018
57,962.86	76.86	14.810	0.037	13.297	0.033	12.636	0.029	12.233	0.019
57,964.86	78.86	14.797	0.008	13.325	0.005	12.657	0.003	12.252	0.004
57,965.94	79.94	14.818	0.008	13.333	0.005	12.675	0.003	12.245	0.004
57,966.92	80.92	14.821	0.008	13.332	0.005	12.669	0.003	12.257	0.004
57,967.87	81.87	14.858	0.062	13.376	0.032	12.660	0.034	12.257	0.019
57,968.88	82.88	14.888	0.025	13.356	0.026	12.658	0.027	12.235	0.039
57,970.89	84.89	14.905	0.064	13.382	0.033	12.693	0.025	12.268	0.022
57,972.88	86.88	14.961	0.038	13.417	0.021	12.692	0.014	12.282	0.020
57,973.86	87.86	14.977	0.046	13.410	0.025	12.692	0.022	12.278	0.020
57,974.86	88.86	14.989	0.041	13.422	0.030	12.716	0.018	12.291	0.025
57,976.00	90.00	15.011	0.046	13.422	0.016	12.727	0.024	12.294	0.014
57,980.02	94.02	15.117	0.041	13.523	0.032	12.766	0.028	12.349	0.030
57,982.84	96.84	15.192	0.031	13.555	0.028	12.778	0.029	12.367	0.021
57,983.85	97.85	15.229	0.032	13.583	0.019	12.813	0.029	12.383	0.023
57,986.86	100.86	15.340	0.034	13.648	0.019	12.874	0.019	12.437	0.016
57,987.92	101.92	15.337	0.012	13.694	0.007	12.909	0.004	12.466	0.004
57,988.84	102.84	15.418	0.032	13.718	0.024	12.923	0.023	12.484	0.021
57,993.81	107.81	15.647	0.042	13.925	0.024	13.088	0.020	12.622	0.025
57,994.88	108.88	15.768	0.059	13.980	0.044	13.136	0.031	12.673	0.033
57,995.88	109.88	15.818	0.058	14.051	0.043	13.178	0.022	12.700	0.018
58,000.83	114.83	16.202	0.068	14.384	0.030	13.470	0.016	12.963	0.048
58,006.81	120.81	16.880	0.056	15.084	0.032	14.051	0.035	13.505	0.025
58,011.80	125.80	17.385	0.048	15.530	0.027	14.434	0.019	13.858	0.020
58,022.92	136.92	17.779	0.048	15.679	0.031	14.561	0.019	14.024	0.011
58,023.92	137.92	17.540	0.037	15.698	0.029	14.603	0.030	14.048	0.019
58,024.82	138.82	17.617	0.037	15.725	0.026	14.617	0.022	14.049	0.019
58,025.80	139.80	17.564	0.041	15.754	0.021	14.620	0.024	14.053	0.021
58,026.88	140.88	17.672	0.015	15.761	0.011	14.655	0.015	14.048	0.012
58,027.83	141.83	17.648	0.022	15.816	0.009	14.677	0.019	14.076	0.013
58,032.75	146.75	17.615	0.025	15.809	0.024	14.695	0.008	14.099	0.006
58,035.75	149.75	17.661	0.019	15.886	0.009	14.736	0.011	14.143	0.013
58,040.81	154.81	17.684	0.044	15.899	0.025	14.818	0.026	14.211	0.020
58,041.84	155.84	17.679	0.012	15.916	0.013	14.781	0.011	14.181	0.011
58,044.79	158.79	17.678	0.056	15.906	0.027	14.828	0.029	14.217	0.022
58,046.72	160.72	17.798	0.035	15.944	0.025	14.815	0.025	14.258	0.015
58,050.70	164.70	17.771	0.047	15.973	0.024	14.884	0.017	14.276	0.021
58,055.95	169.95	17.768	0.038	16.069	0.026	14.871	0.017	14.314	0.023
58,063.89	177.89	17.901	0.018	16.131	0.015	14.964	0.010	14.364	0.008
58,064.81	178.81	17.841	0.031	16.139	0.023	14.948	0.006	14.368	0.006
58,075.80	189.80	17.874	0.072	16.221	0.031	15.110	0.031	14.729	0.064
58,094.79	208.79	18.083	0.054	16.407	0.030	15.235	0.025	14.674	0.028
58,182.12	296.12	18.659	0.077	17.330	0.046	16.191	0.031	15.620	0.027

Table 5
LCO $UBVg'r'i'$ Photometry of SN 2017eaw

Date (MJD)	Epoch (days)	U (mag)	B (mag)	V (mag)	g' (mag)	r' (mag)	i' (mag)
57,888.85	2.85	12.523(0.014)	13.222(0.012)	12.992(0.022)	12.760(0.018)	12.903(0.013)	12.880(0.023)
57,889.91	3.91	...	13.198(0.011)	12.888(0.015)	12.698(0.010)	12.774(0.012)	12.752(0.015)
57,891.93	5.93	12.431(0.012)	13.148(0.019)	12.807(0.016)	12.653(0.018)	12.653(0.019)	12.573(0.015)
57,893.82	7.82	12.394(0.025)	13.128(0.007)	12.774(0.015)	12.656(0.022)	12.591(0.024)	12.500(0.012)
57,895.91	9.91	...	13.146(0.009)	12.855(0.022)	12.699(0.012)	12.612(0.016)	12.556(0.035)
57,896.89	10.89	12.467(0.018)	13.173(0.014)	12.868(0.013)	12.703(0.020)	12.580(0.010)	12.542(0.010)
57,897.81	11.81	...	13.229(0.012)	12.869(0.022)	12.731(0.011)	12.593(0.016)	12.557(0.016)
57,898.83	12.83	12.655(0.017)	13.257(0.017)	12.888(0.011)	12.769(0.015)	12.613(0.012)	12.583(0.018)
57,902.81	16.81	12.886(0.012)	13.374(0.038)	12.933(0.029)	12.862(0.015)	12.634(0.011)	12.620(0.014)
57,906.82	20.82	...	13.476(0.022)	12.945(0.013)	12.868(0.019)	12.582(0.023)	12.619(0.046)
57,907.86	21.86	13.344(0.013)	13.536(0.019)	12.868(0.013)	12.911(0.032)	12.583(0.010)	12.555(0.023)
57,908.87	22.87	13.491(0.035)	13.581(0.020)	12.924(0.011)	12.939(0.027)	12.597(0.011)	12.535(0.018)
57,909.85	23.85	13.601(0.034)	13.638(0.011)	12.920(0.010)	12.977(0.010)	12.608(0.025)	12.596(0.011)
57,910.88	24.88	12.995(0.010)	12.984(0.023)	12.643(0.015)	12.600(0.019)
57,916.89	30.89	13.178(0.011)	12.669(0.018)	12.593(0.010)
57,917.84	31.84	...	13.981(0.014)	13.037(0.014)	13.200(0.011)	12.673(0.018)	12.586(0.012)
57,928.79	42.79	14.879(0.030)	14.281(0.017)	13.169(0.015)	13.418(0.010)	12.782(0.010)	12.685(0.010)
57,934.82	48.82	15.146(0.030)	14.373(0.026)	13.164(0.014)	13.477(0.015)	12.769(0.032)	12.614(0.029)
57,940.84	54.84	15.426(0.019)	14.447(0.012)	13.159(0.012)	13.448(0.010)	12.774(0.014)	12.611(0.016)
57,944.80	58.80	15.493(0.018)	14.513(0.015)	13.193(0.011)	13.524(0.012)	12.791(0.008)	...
57,945.84	59.84	15.522(0.023)	14.543(0.016)	13.185(0.014)	13.552(0.013)	12.805(0.018)	12.606(0.025)
57,961.83	75.83	16.014(0.051)	14.699(0.018)	13.221(0.011)	13.683(0.012)	12.821(0.011)	12.640(0.015)
57,965.93	79.93	...	14.834(0.054)
57,971.87	85.87	16.425(0.047)	14.902(0.016)	13.340(0.012)	13.789(0.013)	12.850(0.018)	12.625(0.026)
57,972.83	86.83	16.392(0.037)	14.902(0.014)	13.345(0.014)	13.831(0.020)	12.875(0.013)	12.668(0.005)
57,976.80	90.80	16.641(0.016)	15.015(0.018)	13.408(0.019)	13.901(0.036)	12.979(0.023)	12.716(0.013)
57,995.81	109.81	17.756(0.028)	15.747(0.027)	13.907(0.038)	14.593(0.012)	13.315(0.019)	13.055(0.013)
58,001.74	115.74	...	16.267(0.018)	14.430(0.012)	15.095(0.028)	13.716(0.012)	13.410(0.026)
58,002.84	116.84	...	16.375(0.039)	14.489(0.016)	15.158(0.017)	13.777(0.018)	13.513(0.017)
58,004.81	118.81	...	16.629(0.017)	14.768(0.022)	15.403(0.026)	13.974(0.011)	13.678(0.016)
58,005.82	119.82	...	16.719(0.043)	14.868(0.013)	15.589(0.015)	14.099(0.013)	13.834(0.012)
58,008.82	122.82	...	17.123(0.022)	15.289(0.021)	15.935(0.036)	14.405(0.018)	14.131(0.048)
58,009.80	123.80	...	17.247(0.028)	15.379(0.018)
58,010.83	124.83	...	17.334(0.016)	15.395(0.011)	16.136(0.012)	14.597(0.015)	14.287(0.028)
58,018.78	132.78	...	17.535(0.026)	15.651(0.015)	16.361(0.015)	14.793(0.027)	14.481(0.013)
58,019.77	133.77	...	17.502(0.014)	15.669(0.024)	16.383(0.017)	14.786(0.014)	14.457(0.022)
58,028.75	142.75	...	17.611(0.023)	15.756(0.022)	16.444(0.015)	14.838(0.010)	14.557(0.006)
58,034.76	148.76	...	17.710(0.025)	15.823(0.037)	16.450(0.030)	14.900(0.018)	14.645(0.025)
58,035.73	149.73	...	17.630(0.028)	15.781(0.022)	16.495(0.021)	14.884(0.012)	14.668(0.021)
58,039.75	153.75	...	17.687(0.017)	15.831(0.012)	16.583(0.010)	14.960(0.011)	14.722(0.041)
58,043.73	157.73	...	17.703(0.013)	15.868(0.014)	16.588(0.013)	14.992(0.018)	14.735(0.012)
58,047.60	161.60	...	17.710(0.019)	15.929(0.013)
58,051.62	165.62	...	17.747(0.034)	15.970(0.020)	16.674(0.010)	15.038(0.020)	14.809(0.013)
58,055.59	169.59	...	17.801(0.029)	16.028(0.020)	16.679(0.010)	15.096(0.028)	14.833(0.014)
58,059.66	173.66	...	17.824(0.023)	16.061(0.010)	16.681(0.011)	15.088(0.020)	14.882(0.015)
58,060.65	174.65	...	17.760(0.029)	16.032(0.010)	16.679(0.018)	15.114(0.012)	14.900(0.012)
58,071.62	185.62	...	17.843(0.112)	16.045(0.036)	16.809(0.016)	15.132(0.028)	14.977(0.013)
58,082.57	196.57	...	17.955(0.023)	16.298(0.015)	16.880(0.016)	15.302(0.018)	15.132(0.020)
58,099.57	213.57	...	17.997(0.022)	16.449(0.029)	16.984(0.015)	15.460(0.011)	15.301(0.015)
58,231.02	345.02	...	19.012(0.033)	17.819(0.014)	18.064(0.013)	16.933(0.025)	16.623(0.017)
58,246.05	360.05	17.984(0.026)	18.167(0.021)	17.136(0.019)	16.820(0.046)
58,246.83	360.83	...	19.065(0.040)	17.958(0.060)	18.153(0.029)	17.131(0.062)	16.793(0.018)
58,255.02	369.02	...	19.134(0.014)	18.030(0.010)	18.249(0.026)	17.245(0.037)	16.906(0.031)
58,258.81	372.81	...	19.180(0.023)	18.086(0.011)	18.326(0.022)	17.374(0.028)	16.986(0.010)
58,267.92	381.92	18.253(0.027)	18.487(0.038)	17.466(0.034)	17.142(0.051)
58,284.78	398.78	...	19.453(0.018)	18.354(0.014)	18.632(0.015)	17.666(0.044)	17.345(0.041)
58,292.77	406.77	...	19.521(0.032)	18.506(0.034)	...	17.769(0.013)	17.390(0.016)
58,318.75	432.75	...	19.783(0.021)	18.784(0.011)	18.909(0.048)	18.175(0.017)	17.768(0.022)
58,335.90	449.90	...	19.976(0.059)	19.045(0.022)	19.204(0.033)	18.381(0.019)	...
58,351.74	465.74	...	20.092(0.086)	19.230(0.013)	19.397(0.047)	18.631(0.023)	18.208(0.012)
58,374.81	488.81	...	20.371(0.014)	19.434(0.025)	19.645(0.043)	18.876(0.034)	18.673(0.026)
58,385.76	499.76	19.659(0.028)	19.804(0.032)	19.087(0.026)	18.787(0.012)
58,392.72	506.72	...	20.574(0.042)	19.757(0.053)	19.875(0.015)	19.233(0.014)	18.892(0.041)

Table 5
(Continued)

Date (MJD)	Epoch (days)	U (mag)	B (mag)	V (mag)	g' (mag)	r' (mag)	i' (mag)
58,394.63	508.63	...	20.631(0.023)	19.699(0.086)	19.860(0.047)	19.316(0.019)	19.039(0.021)
58,399.68	513.68	19.771(0.011)	19.907(0.048)
58,405.74	519.74	19.959(0.116)	20.069(0.031)	19.386(0.022)	19.215(0.075)
58,417.67	531.67	19.590(0.071)	19.341(0.016)
58,426.55	540.55	20.159(0.025)	20.405(0.021)	19.711(0.036)	19.594(0.012)




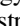

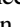






Table 6
Swift Photometry of SN 2017eaw














Date (MJD)	Epoch (days)	$UVW2$ (mag)	$\sigma UVW2$ (mag)	$UVM2$ (mag)	$\sigma UVM2$ (mag)	$UVW1$ (mag)	$\sigma UVW1$ (mag)	U (mag)	σU (mag)	B (mag)	σB (mag)	V (mag)	σV (mag)
57,887.59	1.59	12.378	0.008	12.556	0.007	12.266	0.009	12.239	0.012	13.287	0.012	13.154	0.020
57,887.92	1.92	12.453	0.052	12.579	0.019
57,888.66	2.66	12.666	0.040	12.645	0.011
57,888.80	2.80	12.662	0.013	12.322	0.007
57,889.86	3.86	12.833	0.014
57,890.12	4.12	13.037	0.045	12.877	0.008
57,891.85	5.85	13.423	0.074	13.199	0.010
57,897.55	11.55	14.529	0.016
57,899.42	13.42	14.986	0.026
57,902.08	16.08	15.368	0.036	15.807	0.059	14.153	0.028	12.884	0.019	13.363	0.020	12.976	0.022
57,902.27	16.27	15.304	0.164	15.900	0.042
57,904.06	18.06	15.958	0.033	16.565	0.063	14.584	0.023	13.162	0.014	13.432	0.013	12.970	0.015
57,906.59	20.59	16.445	0.044	17.277	0.085	15.153	0.031	13.533	0.015	13.513	0.014	12.947	0.015
57,908.45	22.45	16.647	0.047	17.748	0.121	15.491	0.036	13.835	0.016	13.593	0.013	12.989	0.015
57,910.18	24.18	16.859	0.052	17.978	0.125	15.591	0.037	14.075	0.017	13.690	0.013	13.029	0.015
57,912.69	26.69	17.033	0.058	18.454	0.194	15.936	0.046	14.357	0.020	13.799	0.014	13.049	0.015
57,914.29	28.29	17.223	0.066	18.890	0.273	16.051	0.047	14.527	0.021	13.889	0.014	13.050	0.015
57,916.89	30.89	16.194	0.051	14.765	0.024	13.936	0.016
57,918.82	32.82	17.456	0.091	18.557	0.211	16.406	0.071	14.965	0.032	14.005	0.017	13.092	0.019
57,920.80	34.80	17.573	0.080	18.753	0.236	16.457	0.058	15.105	0.026	14.099	0.014	13.164	0.015
57,949.17	63.17	18.146	0.090	20.463	0.552	17.148	0.063	16.266	0.044	14.574	0.015	13.272	0.014
57,962.59	76.59	18.357	0.102	21.193	0.892	17.288	0.067	16.741	0.060	14.745	0.016	13.337	0.014
57,977.93	91.93	19.146	0.365	17.843	0.121	17.252	0.102	15.010	0.024	13.599	0.032
57,981.18	95.18	18.947	0.242	19.932	0.428	17.706	0.144	17.455	0.148	15.080	0.027	13.572	0.024
57,990.30	104.30	18.939	0.155	20.653	0.530	18.195	0.123	17.850	0.124	15.463	0.021	13.864	0.017
58,004.65	118.65	20.535	0.596	18.589	0.170	19.090	0.343	16.661	0.043	14.942	0.038
58,009.43	123.43	20.249	0.728	18.974	0.416	18.912	0.466	17.254	0.101	15.497	0.066

Table 7
Log of Spectroscopic Observations

UT Date	Phase (days)	Instrument	Range (Å)	R ($\lambda/\Delta\lambda$)
2017 May 15	+3	<i>Swift</i> UVOT/UGRISM	2000–5000	150
2017 May 16	+3	HET LRS2	3700–10500	1100/1800/1900
2017 May 16	+3	LCO FLOYDS	3250–10000	400–700
2017 May 18	+5	LCO FLOYDS	3250–10000	400–700
2017 May 19	+6	HET LRS2	3700–10500	1100/1800/1900
2017 May 19	+6	LCO FLOYDS	3250–10000	400–700
2017 May 19	+6	IRTF SpeX	8000–24000	1200
2017 May 21	+8	LCO FLOYDS	3250–10000	400–700
2017 May 22	+10	<i>Swift</i> UVOT/UGRISM	2000–5000	150
2017 May 23	+10	HET LRS2	3700–10500	1100/1800/1900
2017 May 23	+10	LCO FLOYDS	3250–10000	400–700
2017 May 24	+11	IRTF SpeX	8000–24000	1200
2017 May 25	+12	LCO FLOYDS	3250–10000	400–700
2017 May 27	+14	LCO FLOYDS	3250–10000	400–700
2017 May 31	+18	LCO FLOYDS	3250–10000	400–700
2017 Jun 2	+20	LCO FLOYDS	3250–10000	400–700
2017 Jun 3	+21	HET LRS2	3700–10500	1100/1800/1900
2017 Jun 3	+21	LCO FLOYDS	3250–10000	400–700
2017 Jun 5	+23	LCO FLOYDS	3250–10000	400–700
2017 Jun 8	+26	IRTF SpeX	8000–24000	1200
2017 Jun 14	+32	HET LRS2	3700–10500	1100/1800/1900
2017 Jun 21	+39	IRTF SpeX	8000–24000	1200
2017 Jun 24	+42	LCO FLOYDS	3250–10000	400–700
2017 Jul 1	+49	LCO FLOYDS	3250–10000	400–700
2017 Jul 6	+54	LCO FLOYDS	3250–10000	400–700
2017 Jul 8	+56	IRTF SpeX	8000–24000	1200
2017 Jul 8	+56	Lick Shane/Kast	3250–10000	600
2017 Jul 13	+61	LCO FLOYDS	3250–10000	400–700
2017 Jul 24	+72	LCO FLOYDS	3250–10000	400–700
2017 Jul 27	+75	LCO FLOYDS	3250–10000	400–700
2017 Jul 30	+78	HET LRS2	3700–10500	1100/1800/1900
2017 Aug 4	+83	LCO FLOYDS	3250–10000	400–700
2017 Aug 10	+89	LCO FLOYDS	3250–10000	400–700
2017 Aug 16	+95	LCO FLOYDS	3250–10000	400–700
2017 Aug 24	+103	LCO FLOYDS	3250–10000	400–700
2017 Aug 28	+107	HET LRS2	3700–10500	1100/1800/1900
2017 Sep 15	+125	LCO FLOYDS	3250–10000	400–700
2017 Sep 15	+125	Keck LRIS	3115–10235	300–5000
2017 Sep 21	+131	HET LRS2	3700–10500	1100/1800/1900
2017 Sep 22	+132	LCO FLOYDS	3250–10000	400–700
2017 Sep 26	+136	LCO FLOYDS	3250–10000	400–700
2017 Oct 22	+162	HET LRS2	3700–10500	1100/1800/1900
2017 Dec 19	+220	Keck LRIS	3115–10235	300–5000
2018 Jul 22	+435	Gemini-North GMOS-N	3800–10000	500
2018 Sep 16	+490	Gemini-North GMOS-N	3800–10000	500

ORCID iDs

Tamás Szalai  <https://orcid.org/0000-0003-4610-1117>
 József Vinkó  <https://orcid.org/0000-0001-8764-7832>
 Andrea P. Nagy  <https://orcid.org/0000-0002-9324-3903>
 K. Azalee Bostroem  <https://orcid.org/0000-0002-4294-444X>
 Krisztián Sárneczky  <https://orcid.org/0000-0003-0926-3950>
 Peter J. Brown  <https://orcid.org/0000-0001-6272-5507>
 Ondrej Pejcha  <https://orcid.org/0000-0003-2512-2170>
 Attila Bódi  <https://orcid.org/0000-0002-8585-4544>
 Ottó Hanyecz  <https://orcid.org/0000-0002-9415-5219>
 András Pál  <https://orcid.org/0000-0001-5449-2467>
 Róbert Szakáts  <https://orcid.org/0000-0002-1698-605X>
 Krisztián Vida  <https://orcid.org/0000-0002-6471-8607>

Iair Arcavi  <https://orcid.org/0000-0001-7090-4898>
 Lluís Galbany  <https://orcid.org/0000-0002-1296-6887>
 Daichi Hiramatsu  <https://orcid.org/0000-0002-1125-9187>
 Griffin Hosseinzadeh  <https://orcid.org/0000-0002-0832-2974>
 Eric Y. Hsiao  <https://orcid.org/0000-0003-1039-2928>
 D. Andrew Howell  <https://orcid.org/0000-0003-4253-656X>
 Curtis McCully  <https://orcid.org/0000-0001-5807-7893>
 Jeonghee Rho  <https://orcid.org/0000-0003-3643-839X>
 David J. Sand  <https://orcid.org/0000-0003-4102-380X>
 Melissa Shahbandeh  <https://orcid.org/0000-0002-9301-5302>
 Stefano Valenti  <https://orcid.org/0000-0001-8818-0795>
 Xiaofeng Wang  <https://orcid.org/0000-0002-7334-2357>
 J. Craig Wheeler  <https://orcid.org/0000-0003-1349-6538>

References

- Anand, G. S., Rizzi, L., & Tully, R. B. 2018, *AJ*, **156**, 105
- Argo, M., Torres, M. P., Beswick, R., & Wrigley, N. 2017a, *ATel*, **10421**, 1
- Argo, M., Torres, M. P., Beswick, R., & Wrigley, N. 2017b, *ATel*, **10472**, 1
- Arnett, W. D., & Fu, A. 1989, *ApJ*, **340**, 396
- Astropy Collaboration, Robitaille, T. P., Tollerud, E. J., et al. 2013, *A&A*, **558**, A33
- Bayless, A. J., Pritchard, T. A., Roming, P. W. A., et al. 2013, *ApJL*, **764**, L13
- Bertin, E., & Arnouts, S. 1996, *A&AS*, **117**, 393
- Blinnikov, S. I., Eastman, R., Bartunov, O. S., Popolitov, V. A., & Woosley, S. E. 1998, *ApJ*, **496**, 454
- Blinnikov, S. I., Lundqvist, P., Bartunov, O., Nomoto, K., & Iwamoto, K. 2000, *ApJ*, **532**, 1132
- Blinnikov, S. I., Röpke, F. K., Sorokina, E. I., et al. 2006, *A&A*, **453**, 229
- Blondin, S., Prieto, J. L., Patat, F., et al. 2009, *ApJ*, **693**, 207
- Bose, S., Kumar, B., Sutaria, F., et al. 2013, *MNRAS*, **433**, 1871
- Branch, D., Baron, E. A., & Jeffery, D. J. 2003, in *Supernovae and Gamma-Ray Bursters*, ed. K. W. Weiler (Berlin: Springer), 47
- Breeveld, A. A., Landsman, W., Holland, S. T., et al. 2011, in *AIP Conf. Ser., Gamma Ray Bursts 2010*, 1358 (Melville, NY: AIP), 373
- Bright, J., Mooley, K. P., Fender, R. P., & Horesh, A. 2017, *ATel*, **10394**, 1
- Brown, P. J., Breeveld, A., Roming, P. W. A., & Siegel, M. 2016, *AJ*, **152**, 102
- Brown, P. J., Roming, P. W. A., Milne, P., et al. 2010, *ApJ*, **721**, 1608
- Bullivant, C., Smith, N., Williams, G. G., et al. 2018, *MNRAS*, **476**, 1497
- Burrows, D. N., Hill, J. E., Nousek, J. A., et al. 2005, *SSRv*, **120**, 165
- Chakraborti, S., Ray, A., Smith, R., et al. 2016, *ApJ*, **817**, 22
- Cheng, Y.-C., Chen, T.-W., & Prentice, S. 2017, *ATel*, **10374**, 1
- Chevalier, R. A., & Fransson, C. 2003, *LNP Supernovae and Gamma-Ray Bursters*, **598**, 171
- Chevalier, R. A., & Fransson, C. 2017, in *Handbook of Supernovae*, ed. A. W. Alsabti & P. Murdin (Berlin: Springer), 875
- Chevalier, R. A., Fransson, C., & Nyman, T. K. 2006, *ApJ*, **641**, 1029
- Chonis, T. S., Hill, G. J., Lee, H., et al. 2016, *Proc. SPIE*, **9908**, 084C
- Cushing, M. C., Vacca, W. D., & Rayner, J. T. 2004, *PASP*, **116**, 362
- D'Andrea, C. B., Sako, M., Dilday, B., et al. 2010, *ApJ*, **708**, 661
- de Jaeger, T., González-Gaitán, S., Hamuy, M., et al. 2017, *ApJ*, **835**, 166
- Dessart, L., & Hillier, D. J. 2005, *A&A*, **439**, 671
- Dessart, L., Hillier, D. J., & Audit, E. 2017, *A&A*, **605**, 83
- Dessart, L., Hillier, D. J., & Wilk, K. D. 2018, *A&A*, **619**, 30
- Dhungana, G., Kehoe, R., Vinkó, J., et al. 2016, *ApJ*, **822**, 6
- Dong, S., & Stanek, K. Z. 2017, *ATel*, **10372**, 1
- Drake, A. J., Djorgovski, S. G., Mahabal, A. A., et al. 2017, *ATel*, **10397**, 1
- Faran, T., Poznanski, D., Filippenko, A. V., et al. 2014, *MNRAS*, **442**, 844
- Fitzpatrick, E. L., & Massa, D. 2007, *ApJ*, **663**, 320
- Friedman, S. D., York, D. G., McCall, B. J., et al. 2011, *ApJ*, **727**, 33
- Fu, A., & Arnett, W. D. 1989, *ApJ*, **340**, 414
- Galbany, L., Hamuy, M., Phillips, M. M., et al. 2016, *AJ*, **151**, 33
- Gall, E. E. E., Kotak, R., Leibundgut, B., et al. 2016, *A&A*, **592**, A129
- Gall, E. E. E., Kotak, R., Leibundgut, B., et al. 2018, *A&A*, **611**, A25
- Gal-Yam, A., Bufano, F., Barlow, T. A., et al. 2008, *ApJL*, **685**, L117
- Garnavich, P. M., Tucker, B. E., Rest, A., et al. 2016, *ApJ*, **820**, 23
- Gehrels, N., Chincarini, G., Giommi, P., et al. 2004, *ApJ*, **611**, 1005
- Gimeno, G., Roth, K., Chiboucas, K., et al. 2016, *Proc. SPIE*, **9908**, 99082S
- Grefenstette, B., Harrison, F., & Brightman, M. 2017, *ATel*, **10427**, 1
- Grupe, D., Dong, S., Shappee, B. J., et al. 2016, *ATel*, **8588**, 1
- Gutiérrez, C. P., Anderson, J. P., Hamuy, M., et al. 2017, *ApJ*, **850**, 89
- Hamuy, M., & Pinto, P. A. 2002, *ApJL*, **566**, L63
- Henden, A. A., Levine, S., & Terrell, D. 2015, *AAS Meeting Abstracts*, **225**, 336.16
- Herrmann, K. A., Ciardullo, R., Feldmeier, J. J., & Vinciguerra, M. 2008, *ApJ*, **683**, 630
- Hook, I. M., Jørgensen, I., Allington-Smith, J. R., et al. 2004, *PASP*, **116**, 425
- Hosseinzadeh, G., Valenti, S., McCully, C., et al. 2018, *ApJ*, **861**, 63
- Hsiao, E. Y., Phillips, M. M., Marion, G. H., et al. 2019, *PASP*, **131**, 014002
- Huang, F., Wang, X.-F., Hosseinzadeh, G., et al. 2018, *MNRAS*, **475**, 3959
- Immler, S., Brown, P. J., Milne, P., et al. 2007, *ApJ*, **664**, 435
- Jerkstrand, A., Fransson, C., & Kozma, C. 2011, *A&A*, **530**, A45
- Jerkstrand, A., Fransson, C., Maguire, K., et al. 2012, *A&A*, **546**, A28
- Jerkstrand, A., Smartt, S. J., Fraser, M., et al. 2014, *MNRAS*, **439**, 3694
- Johnson, S. A., Kochanek, C. S., & Adams, S. M. 2018, *MNRAS*, **480**, 1696
- Khan, R. 2017, *ATel*, **10373**, 1
- Khazov, D., Yaron, O., Gal-Yam, A., et al. 2016, *ApJ*, **818**, 3
- Kilpatrick, C. D., & Foley, R. J. 2018, *MNRAS*, **481**, 2536
- Kochanek, C. S., Khan, R., & Dai, X. 2012, *ApJ*, **759**, 20
- Kong, A. K. H., & Li, K. L. 2017, *ATel*, **10380**, 1
- Kotak, R., Meikle, W. P. S., van Dyk, S. D., Höflich, P. A., & Mattila, S. 2005, *ApJL*, **628**, L123
- Landolt, A. U. 1992, *AJ*, **104**, 340
- Li, W., Van Dyk, S. D., Filippenko, A. V., & Cuillandre, J.-C. 2005, *PASP*, **117**, 121
- Li, W., Wang, X., Vinkó, J., et al. 2019, *ApJ*, **870**, 12
- Maguire, K., Di Carlo, E., Smartt, S. J., et al. 2010, *MNRAS*, **404**, 981
- Maguire, K., Kotak, R., Smartt, S. J., et al. 2010, *MNRAS*, **403**, L11
- McCarthy, J. K., Cohen, J. G., Butcher, B., et al. 1998, *Proc. SPIE*, **3355**, 81
- Misra, K., George, K., Dastidar, R., & Gangopadhyay, A. 2017, *ATel*, **10501**, 1
- Misra, K., Pooley, D., Chandra, P., et al. 2007, *MNRAS*, **381**, 280
- Mooley, K. P., Cantwell, T., Titterton, D. J., et al. 2017, *ATel*, **10413**, 1
- Moriya, T. J., Förster, F., Yoon, S.-C., Gräfener, G., & Blinnikov, S. I. 2018, *MNRAS*, **476**, 2840
- Moriya, T. J., Tominaga, N., Blinnikov, S. I., Baklanov, P. V., & Sorokina, E. I. 2011, *MNRAS*, **415**, 199
- Moriya, T. J., Yoon, S.-C., Gräfener, G., & Blinnikov, S. I. 2017, *MNRAS*, **469**, L108
- Morozova, V., Piro, A. L., & Valenti, S. 2017, *ApJ*, **838**, 28
- Morozova, V., Piro, A. L., & Valenti, S. 2018, *ApJ*, **858**, 15
- Munari, U., & Zwitter, T. 1997, *A&A*, **318**, 269
- Nagy, A. P. 2018, *ApJ*, **862**, 143
- Nagy, A. P., & Vinkó, J. 2016, *A&A*, **589**, A53
- Nakaoka, T., Kawabata, K. S., Maeda, K., et al. 2018, *ApJ*, **859**, 78
- Nayana, A. J., & Chandra, P. 2017a, *ATel*, **10388**, 1
- Nayana, A. J., & Chandra, P. 2017b, *ATel*, **10534**, 1
- Oke, J. B., Cohen, J. G., Carr, M., et al. 1995, *PASP*, **107**, 375
- Olivares, E. F., Hamuy, M., Pignata, G., et al. 2010, *ApJ*, **715**, 833
- Pejcha, O., & Prieto, J. L. 2015, *ApJ*, **806**, 225
- Phillips, M. M., Simon, J. D., Morrell, N., et al. 2013, *ApJ*, **779**, 38
- Pooley, D., Lewin, W. H. G., Fox, D. W., et al. 2002, *ApJ*, **572**, 932
- Poznanski, D., Butler, N., Filippenko, A. V., et al. 2009, *ApJ*, **694**, 1067
- Poznanski, D., Ganeshalingam, M., Silverman, J. M., & Filippenko, A. V. 2011, *MNRAS*, **415**, 81
- Poznanski, D., Nugent, P. E., & Filippenko, A. V., 2010, *ApJ*, **721**, 956
- Poznanski, D., Prochaska, J. X., & Bloom, J. S. 2012, *MNRAS*, **426**, 1465
- Quimby, R. M., Wheeler, J. C., Höflich, P., et al. 2006, *ApJ*, **666**, 1093
- Rayner, J. T., Toomey, D. W., Onaka, P. M., et al. 2003, *PASP*, **115**, 362
- Rho, J., Geballe, T. R., Banerjee, D. P. K., et al. 2018, *ApJL*, **864**, L20
- Rockosi, C., Stover, R., Kibrick, R., et al. 2010, *Proc. SPIE*, **7735**, 77350R
- Roming, P. W. A., Kennedy, T. E., Mason, K. O., et al. 2005, *SSRv*, **120**, 95
- Rui, L., Wang, X., Mo, J., et al. 2019, *MNRAS*, **485**, 1990
- Sahu, D. K., Anupama, G. C., Srividya, S., & Muneer, S. 2006, *MNRAS*, **372**, 1315
- Sárneczky, K., Vida, K., Vinkó, J., & Szalai, T. 2017, *ATel*, **10381**, 1
- Schlafly, E. F., & Finkbeiner, D. 2011, *ApJ*, **737**, 103
- Szalai, T., Vinkó, J., Balog, Z., et al. 2011, *A&A*, **527**, A61
- Szalai, T., Zsíros, S., Fox, O. D., et al. 2018, *ApJS*, in press (arXiv:1803.02571)
- Takáts, K., & Vinkó, J. 2006, *MNRAS*, **372**, 1735
- Takáts, K., & Vinkó, J. 2012, *MNRAS*, **419**, 2783
- Tikhonov, N. A. 2014, *AstL*, **40**, 537
- Tinyant, S., Kasliwal, M., Krafton, K., et al. 2019, *ApJ*, **873**, 127
- Tomasella, L., Benetti, S., Cappellaro, E., et al. 2017, *ATel*, **10377**, 1
- Tsvetkov, D. Y., Shugarov, S. Y., Volkov, I. M., et al. 2018, *AstL*, **44**, 315
- Turatto, M., Benetti, S., & Cappellaro, E. 2003, in *From Twilight to Highlight: The Physics of Supernovae*, ed. W. Hillebrandt & B. Leibundgut (Berlin: Springer), 200
- Vacca, W. D., Cushing, M. C., & Rayner, J. T. 2003, *PASP*, **115**, 389
- Valenti, S., Howell, D. A., Stritzinger, M. D., et al. 2016, *MNRAS*, **459**, 3939
- van Dyk, S., Filippenko, A. V., Fox, O. D., et al. 2017, *ATel*, **10378**, 1
- Vinkó, J., Takáts, K., Szalai, T., et al. 2012, *A&A*, **540**, A93
- Wiggins, P. 2017, *CBET*, **4390**, 1
- Williams, B. F., Hillis, T. J., Murphy, J. W., et al. 2018, *ApJ*, **860**, 39
- Xiang, D., Rui, L., Wang, X., et al. 2017, *ATel*, **10376**, 1
- Yaron, O., Perley, D. A., Gal-Yam, A., et al. 2017, *NatPh*, **3**, 510
- Zwitter, T., Munari, U., & Moretti, S. 2004, *IAUC*, **8413**, 1